

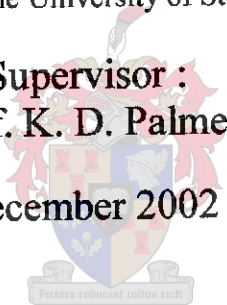
An Active Receiving Antenna for Borehole Pulsed Radar Applications

M. D. van Wyk

(Thesis presented in partial fulfilment of the requirements for the degree of Master of
Engineering at the University of Stellenbosch)

Supervisor :
Prof. K. D. Palmer

December 2002



UNIVERSITEIT • STELLENBOSCH • UNIVERSITY
jou kennisvennoot • your knowledge partner

Chapter 6

ACTIVE RECEIVING ANTENNA

6.1 Introduction

The current radar receiver is based on a $50\ \Omega$ system. From *Chapter 5* (Sections 5.3.4, 5.4.4) has made it evident that a high impedance receiver is more sensitive to frequencies in the desired band (10-100 MHz) for both symmetrical and asymmetrical resistively loaded antennas.

The combination of a high impedance receiver and an electrically small antenna is often referred to as an “active antenna”. An active antenna is normally used for receiving purposes in instances where a normal antenna would be impossible to accommodate physically. This type of antenna is popular with amateur radio systems in the low frequency band. The input impedance of an electrically small antenna is generally capacitive and non-resonant, so that a high impedance load connected to such antenna changes the receiver system from a maximum power transfer system to a voltage detection system. The high impedance will be implemented by using a source follower active amplifier that probes the voltage at the input of the antenna, and in turn delivers output current to a $50\ \Omega$ gain stage.

6.2 Active receiver

This section describes the design and assembly of a full radar receiver system that can be implemented as a borehole radar probe. Section 6.2.1-6.2.3 introduces the optic link that carries the trigger pulse from the transmitter and received pulse from the receiver to the data acquisition system. The optical link is also important because it is non-conductive and does not influence the probe performance as radiators. These sections discuss and characterise the components associated with an optical link and investigate possible methods of improving the performance of the current radar system. Section 6.2.4 contains electromagnetic simulations of the measurement

test in order to predict the receiver gain. This section continues to discuss the receiver components and final assembly of the full system, including the optical link.

6.2.1 Optical modulator

An Agilent HFBR-1404 optical demodulator was used to convert the electrical signal into an optical signal and contains an 820 nm AlGaAs emitter. Figure 6.1 shows the measurement test used to extract the input impedance of the optical diode. From the voltage-current loadline given by the datasheets (Figure 6.2) it is expected that the diode will display a small signal input impedance of 5Ω and a DC resistance of 30Ω .

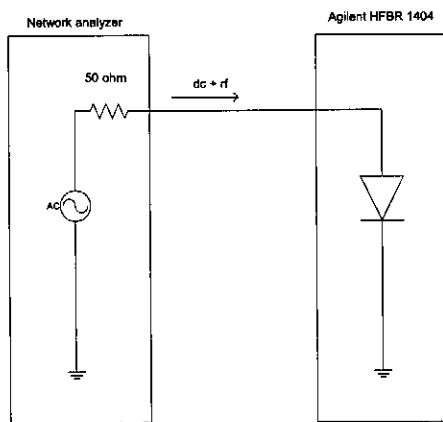


Figure 6.1 : Extracting input impedance of optic modulator diode

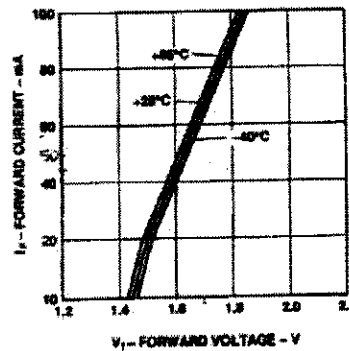


Figure 6.2 : Forward voltage and current characteristics of HFBR 1404 [20]

The diode is linear for a bias current of between 20 mA and 100 mA and the desired bias current ensuring maximum swing without non-linearity will be $60 \text{ mA}_{\text{p-p}}$. The light-emitting diode was biased with a direct current of 60 mA using the internal bias tees of the 8510 vector network analyser. The input resistance (Figure 6.3) varies between 5Ω and 7Ω in the desired bandwidth of 10-100 MHz.

The transmission line between the calibration point of the network analyser and the diode input was negligibly short at these frequencies. The series reactance (Figure 6.4) cannot be due to any

transmission line and must be a function of the diode's input impedance. The reactance dominates over the resistance and some matching network is needed for maximum real power transfer from

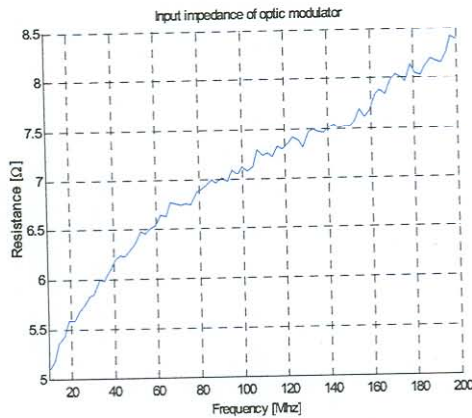


Figure 6.3 : Input resistance of optic modulator diode

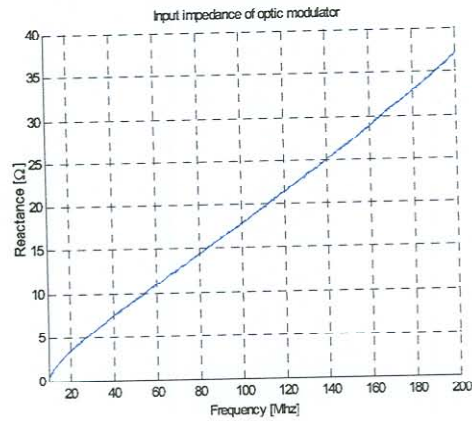


Figure 6.4 : Input reactance of optic modulator diode

the low output real impedance source (voltage source). To design a matching network with a 100 MHz bandwidth is not trivial and some form of impedance inverter is needed to resonate the increasing series inductance over frequency. Since the diode needs to be biased, the optic modulator was incorporated in a discrete transistor circuit, where the quiescent current was used for biasing.

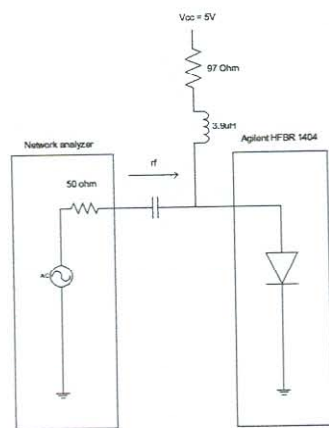


Figure 6.5 : DC bias circuit of optic modulator

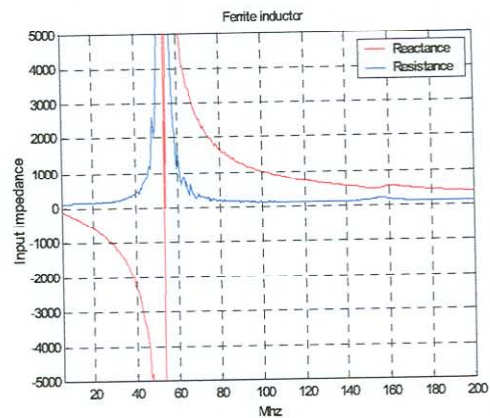


Figure 6.6 : Input impedance of bias inductor

It was decided that the diode could be biased through an inductor and series resistor, as shown in Figure 6.5. This type of biasing is typical for higher frequencies and is easy to implement. The inductor should be chosen so that it resembles a high impedance over the bandwidth in order to resist the signal from leaking through the voltage source. Figure 6.6 gives the measured input impedance of a $3.9 \mu\text{F}$ inductor that was implemented as a choke. The inductor was biased at 65 mA and the ferrite didn't saturate for dc currents up to 112mA. The series resistance regulates the bias current from a 5 V source. The inductor resonates at 55 MHz and produces a high resistance for 10-100 MHz.

6.2.2 Optical demodulator

The optical demodulator (HFBR 2406) unit contains a pin photodiode and a low noise transimpedance pre-amplifier. The receiver output signal is an analogue signal. The unit has to be externally decoupled (Figure 6.7) and has a 125 MHz -3 dB electrical bandwidth.

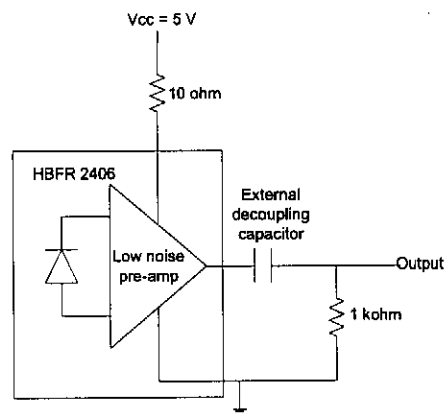


Figure 6.7 : Optic demodulator with external decoupling capacitor and shunted resistor

6.2.3 Optical link

Section 6.2.3.1 introduce a complete optical link and determines the dynamic range. The link was not matched and was driven by a 50Ω signal generator. Efforts to determine the noise floor of the link with an HP 8970B Noise Figure measurement system was unsuccessful. Since matching the

input with a passive element requires difficult filter design, impedance matching incorporating active follower source amplifiers were investigated in section 6.2.3.1. This investigation revealed that the built-in pre-amplifier of the optical demodulator is unable to deliver the current in a low or 50Ω load.

6.2.3.1 Dynamic range of optical fibre link

An optical link was constructed, incorporating an optical modulator and demodulator with a 1m optical fibre (100/140 μm optical fibre). The dynamic range of the optical link was measured on

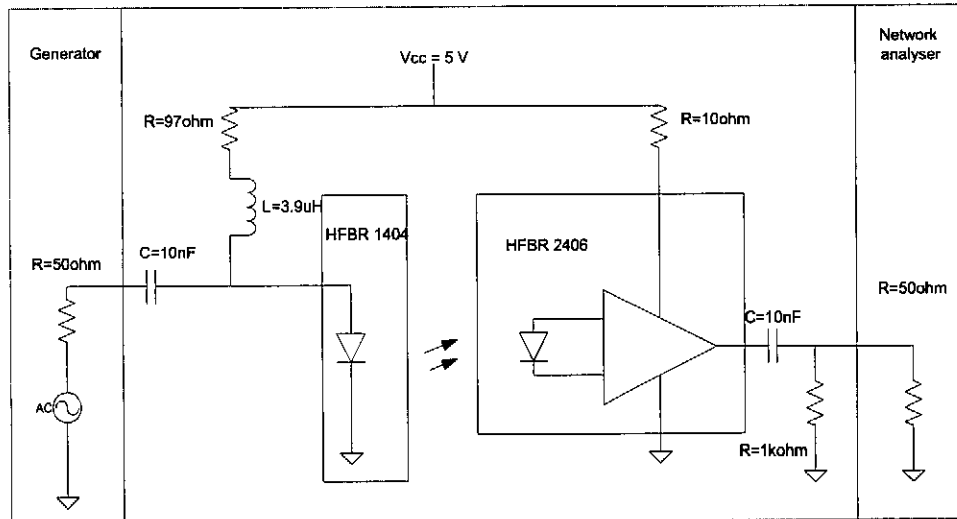


Figure 6.8 : Schematic of dynamic measurement test for optical link

a network analyser (Figure 6.8). The HFBR 1404 was biased at 40mA and 60 mA (Figure 6.9). One measurement was made with -10 dBm input power while the diode was biased through the network analyser ports at 40 mA. This showed that some power leaked through the inductor. At least 50 dBs of dynamic range is possible to obtain with the optical fibre link. The transfer function is not flat and display a 5 dB fall between 10-100 MHz. The link saturates for a power input of 20 dBm (the graph is normalized for a 20 dBm input). No significant change was observed in the noise floor of the network analyser when the optical link was introduced. With low input powers the noise floor of the network analyser starts to dominate.

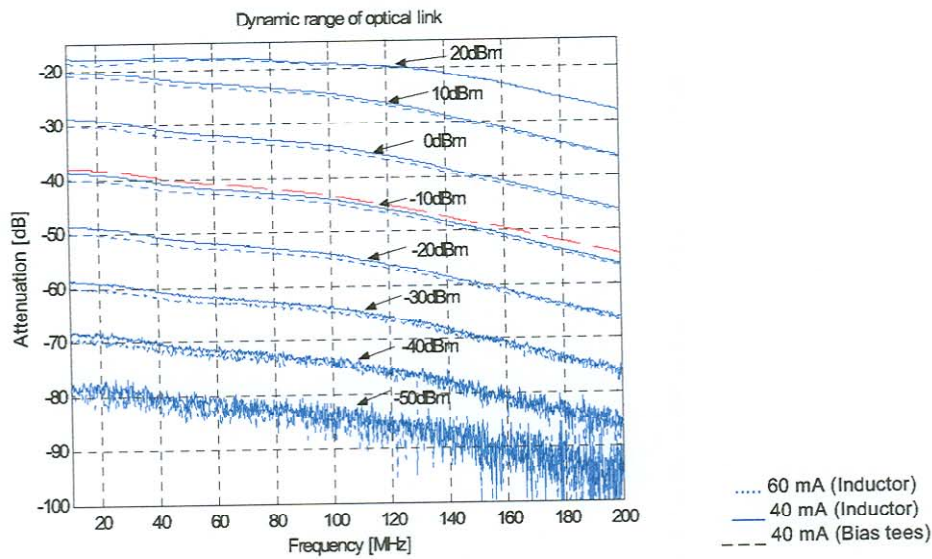


Figure 6.9 : Dynamic range of optical link

Measurements were made on a digitising scope at 15 MHz for various inputs (Figure 6.10). The bias voltage of the optical demodulator is directly proportional to the bias voltage at the optical modulator. This implies that it is not possible to bias the transmitter at 60 mA for a 1m optical fibre, because the signal will saturate at one end. As mentioned before, the receiver is externally decoupled and this bias point of the receiver cannot be shifted.

It was found that 40 mA bias current at the transmitter ensures even saturation at the receiver for a 1m optic fibre cable. This bias current can be higher for longer optical fibre cables, due to DC light attenuation through the cable. Figure 6.10 shows the time traces measured with a voltage probe at the receiver end. The output saturates for a given input ($786 \text{ mV}_{\text{peak}}$) if the receiver is loaded with 50Ω (simulating a network analyser measurement) and the input voltage must be lowered. If the load is removed, the output does not distort (input = $786 \text{ mV}_{\text{peak}}$). This implies that the built-in pre-amplifier of the receiver cannot deliver enough current to drive a low impedance load. Some form of active impedance converter is needed to remedy this deficiency.

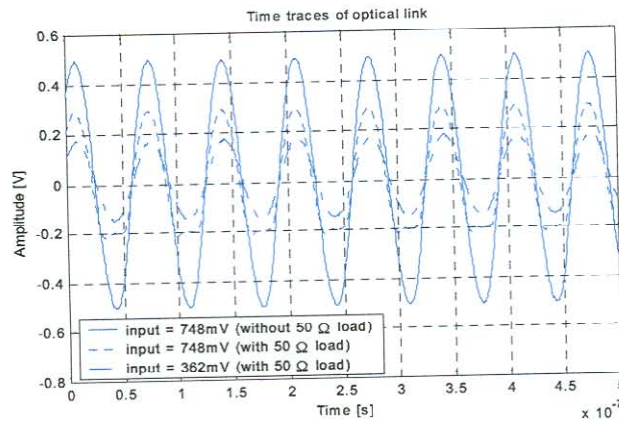


Figure 6.10 : 15 MHz traces measured on a digitised scope for various output loads on the optical link

6.2.3.2 Introducing current feedback amplifiers (Buffers)

A current feedback amplifier or buffer was used to generate a high impedance point at the receiver output to minimize the load on the receiver unit. The buffer had to be able to drive a $50\ \Omega$ load, given the maximum output voltage from the receiver pre-amplifier before saturation. It was initially thought that a buffer could be used to drive the low transmitter resistance, given that it able to supply the low resistance with adequate drive current. Due to the reactance at the high frequencies, it did not deliver good results, as will be seen later.

Two buffers were investigated. The MAX 4200 is a low noise ($2.1\text{ nV}/\sqrt{\text{Hz}}$ noise density) buffer capable of driving $\pm 90\ \text{mA}$ with a $6\ \Omega$ output impedance at 10 MHz. The BUF 601 has a lower output impedance ($3.6\ \Omega$) but can drive only $\pm 20\ \text{mA}$ and has a higher noise density ($4.8\text{ nV}/\sqrt{\text{Hz}}$ noise density). Both buffers were measured on a network analyser with a shunt $50\ \Omega$ resistance at their input. Figures 6.11 and 6.12 show that the MAX 4200 has a flat transfer function with a $-3\ \text{dB}$ bandwidth at 450 MHz, while the BUF 601 display a 1 dB ripple between 10-100MHz. The MAX 4200 was chosen as driver of the optical transmitter due to its high current drive capability and as impedance converter at the output of the optical receiver (Figure 6.13).

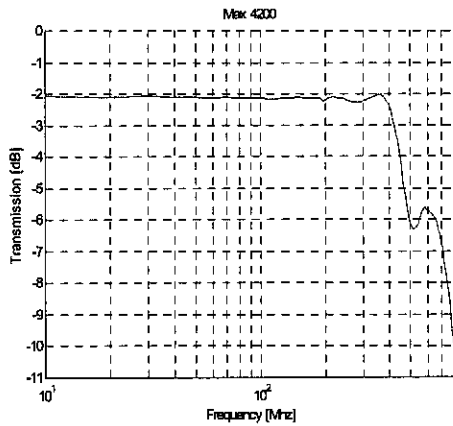


Figure 6.11 : MAX 4200 transfer function

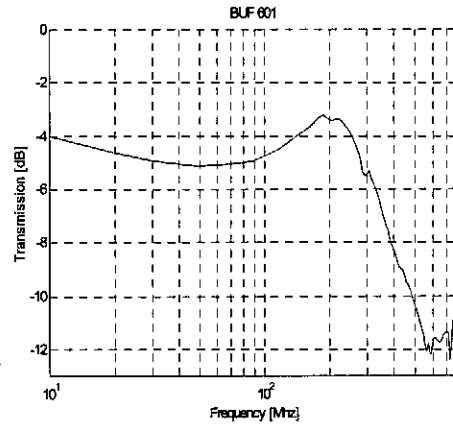


Figure 6.12 : BUF 601 transfer function

The transfer function has a ± 13 dB attenuation between 10-100MHz when the buffer is used to drive the transmitter (Figure 6.14). As discussed before, the reactance dominates the input impedance of the transmitter at the higher frequencies and causes current variations through the

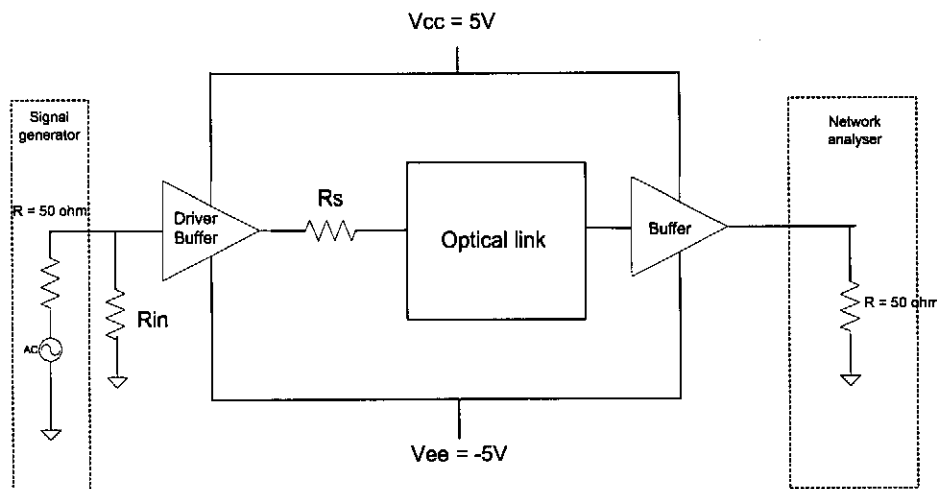


Figure 6.13 : Schematic presentation of buffered optical link

load over frequency. Ideally, a current source with a high source impedance should be used to drive the diode of the transmitter. Variations in the diode impedance will not affect the current. The transfer function flatness improves when only a 50Ω source is used to drive the transmitter. When an output buffer is introduced 2, dBs of gain is added to the overall gain of the link. This gain is attributed to the load-driving capability of the external buffer.

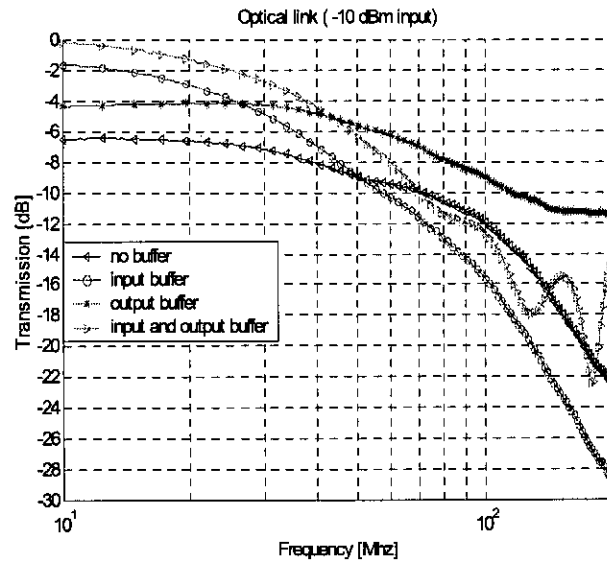


Figure 6.14 : Transfer function of a buffered optical link ($R_{in} = 50 \Omega$, $R_s = 0$)

The input buffer is needed to create a high impedance node at the receiver input to produce a nactive receiver. Choosing $R_s = 50 \Omega$ (input to transmitter (Figure 6.15)) regulates the current through the load and causes a relatively flat transfer function. The flat response is important for a pulsed time domain system if no signal processing is applied to the signal and extra gain will be

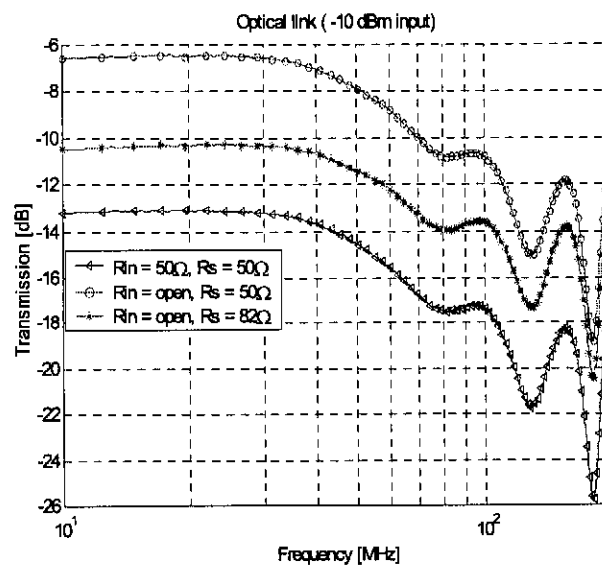


Figure 6.15 : Transfer function of optical link for variable resistor values

added at the output of the buffer, if needed. The important factor is that it is possible to drive the transmitter directly from a 50Ω system, but pay ± 13 dBs of mismatch power (a loss of 20 dBs due to mismatch at driver and a gain of 10 dBs produced by the built-in pre-amplifier of the optic demodulator). When $R_{in} = \infty$ it causes a voltage doubling at the high impedance node created by the input buffer and this accounts for the extra 6 dB of gain.

6.2.4 Active pulse receiver

It was decided that the active receiver would be tested in a controlled open air environment. Section 6.2.4.1 contains electromagnetic simulations of the antenna test in order to establish the receiver gain needed for adequate signal to noise ratio. The amplifiers used for the gain stages are characterised in Section 6.2.4.2 and the transfer function and assembly of the receiver complete with optical link are discussed in Sections 6.2.4.3 and 6.2.4.4. The impulse response of the system to a 10 ns input pulse reveals a low frequency roll-off in section 6.2.4.5.

6.2.4.1 Antenna measurement test and voltage transfer calculations

Making antenna measurements at low frequencies poses problems in terms of unwanted reflections from surrounding objects and the difficulty of ensuring a far-field measurement to eliminate near-field influence. Facilities to measure low frequency antennas are expensive to construct, since the anechoic chamber needs ferrite tiles to absorb the indirect waves. Since these facilities were not attainable at the time of measurement it was decided to take antenna measurements in an open area in air and increase the reception signal to dominate noise from the ambient.

For the pre-calculations, the transmit and receive antennas were considered at a distance of 6m apart. CST[™] calculations were performed on an asymmetric resistively loaded antenna matching the dimensions of the built-system, in order to establish the amount of power transfer. The transmit antenna had a source impedance of $R_{tx} = 1\Omega$ in parallel with the current source, to ensure that a voltage pulse was excited on the antenna. Ideally, the measurement should be conducted in a mine environment to ensure the correct dynamic behaviour on the antennas. Figure

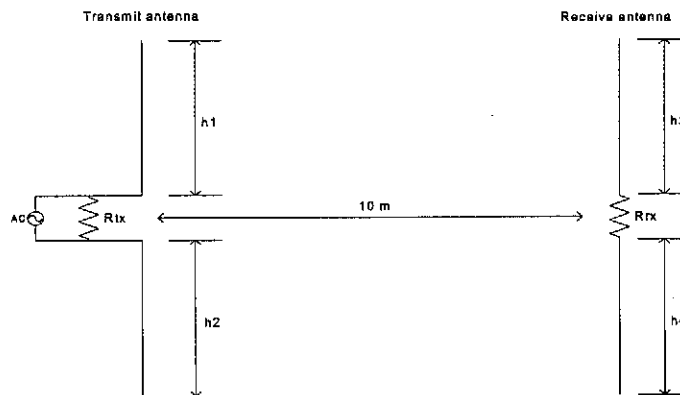


Figure 6.16 : Schematic presentation of simulated transfer between transmitter and receiver ($h_1 = h_2 = 1\text{m}$ (resistive arms), $h_2 = 300\text{mm}$ (ground arm), $h_4 = 420\text{mm}$ (ground arm))

6.16 shows the simulation configuration used to establish the coupling between the transmit and receive antennas. Two asymmetric dipole antennas were considered as transmit and receive antennas in order to establish the minimum and maximum coupling and system amplification needed to conduct the real measurement (Figure 6.17). The resistive arm of the asymmetric dipole had a continuous 100% Wu-King resistive loading (resistor values given by Table 5.1). It was decided to establish the coupling between the antennas by considering the real time input signal at the transmitter and the voltage reception at the receiver. As mentioned before (*Chapter 2*), it is difficult to establish the physical amplitude of the receive pulse by investigating the amplitude energy density spectrums.

Using the time signal, establish a physical feel for the upper limit of the dynamic range expected. Keep in mind that the waveform is dependent on the input pulse (in this case a 2 V Gaussian pulse) and the output peak levels may vary considerably for different transmit pulses of various lengths. In essence, the transmit pulse shape is not as important as transmitting energy over a short period of time. The dynamics of the antenna will also vary the amplitude, depending on the impedance point at the source of the transmitting antenna (whether the transmitting FET closes so fast as to establish second source radiation). In order to minimize the effect that the measurement instrument (digitised scope) will have on the lower limit of the dynamic range, due to internal and external noise, the system will be adapted so that the maximum voltage peak at the receiver will be just below the upper limit of the optic fibre's dynamic range.

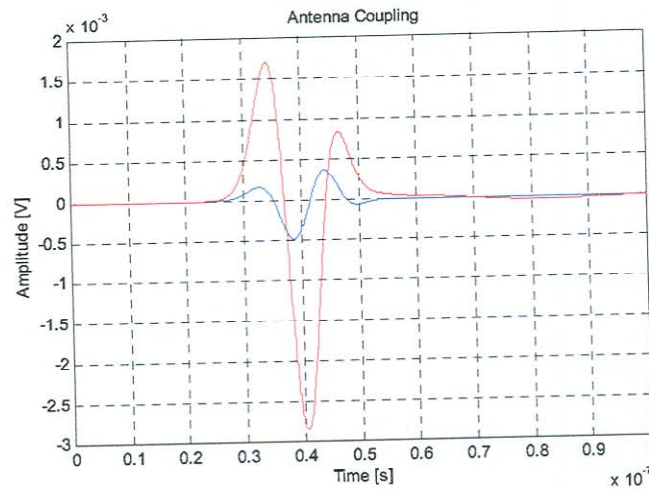


Figure 6.17 : Time trace coupling between transmitter and receiver

The maximum amount of input power into the optical link of Figure 6.9 from a 50Ω source before saturation occurs is 10 dBm, which resembles a $1.4 V_{\text{peak}}$ over the source. This limit may be a few dBs higher after the output buffer is added, but will be chosen as reference for the upper limit of the optical fibre.

The influence of the buffer was omitted for the voltage calculations in Table 6.1. The receiver was thus designed for amplification between the input buffer and optic transmitter. A voltage gain of 52 dB was needed to ensure maximum use of dynamic range for an asymmetric dipole with

Configuration	Input voltage from transmitter [V _{peak}]	Voltage at receive antenna [V _{peak}]	Gain needed to ensure a 1V _{peak} input to optic transmitter
Asymmetric dipole (R _{rx} = 50Ω)	2	0.0005	2000
Asymmetric dipole (R _{rx} = 100kΩ)	2	0.0028	357

Table 6.1 : Receiver amplification calculations

a $100 \text{ k}\Omega$ source resistance. If the digitised scope that would be used to strobe the trace from the receiver does not have enough sensitivity to measure the signal, second amplification before the

scope input would have to be considered. The transmitter peak pulse voltage and duration was adjustable and will be used to prevent saturation.

6.2.4.2 Characterising the gain stages

The availability of high gain video amplifiers limited the options on the components that were implemented to produce additional gain for the receiver. Two amplifiers from *Mini-Circuits* were used to produce the gain stage of the receiver. The MAR-6SM was able to produce the necessary first high gain stage over the video band. MAR-4SM was introduced as the final stage, due to its high power output capabilities, which were necessary to drive the optic modulator. Table 6.2 gives the manufacture specifications for the amplifiers.

Model	Frequency (MHz)	Gain @ 100 MHz	Power output (dBm)	No damage input power (dBm)	Noise figure (dB)
MAR-6SM	0-2000	20	2	13	3
MAR-4SM	0-1000	8	12.5	13	7

Table 6.2 : Amplifier specifications

The amplifiers not only display a low profile, which is needed due to the limited space available in the borehole, but are also low-cost and unconditionally stable and matched to 50Ω . External single (Figure 6.18) rail DC biasing also proves to be an important feature to limit additional components in order to create a differential rail. R_{bias} can be chosen to ensure operation from a 5V source. The s-parameters were measured for the test circuit in Figure 6.18, in order to prove that the amplifiers are stable over the operated frequency band. The MAR-6SM (Figure 6.19) starts to saturate for an input power of -16 dBm. The amplifier displays a gain of ≈ 22 dB between 10-100 MHz and is matched to 50Ω (Figure 6.20).

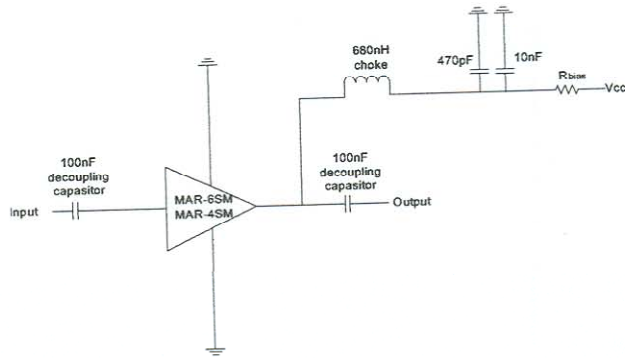


Figure 6.18 : Test bias circuit for MAR amplifiers

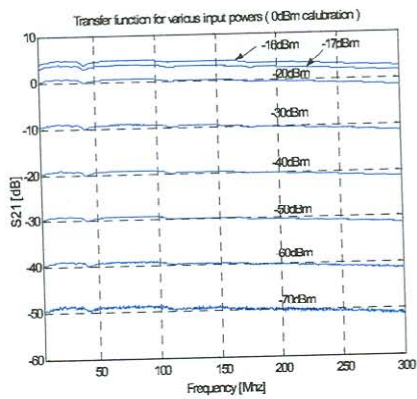


Figure 6.19 : Transfer function of MAR-6SM

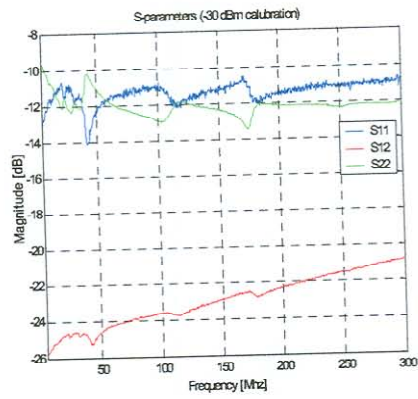


Figure 6.20 : Reverse isolation and impedances of MAR-6SM

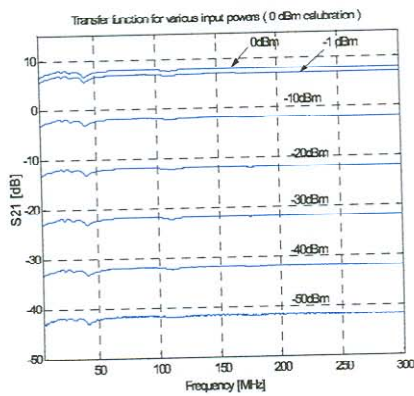


Figure 6.21 : Transfer function of MAR-4SM

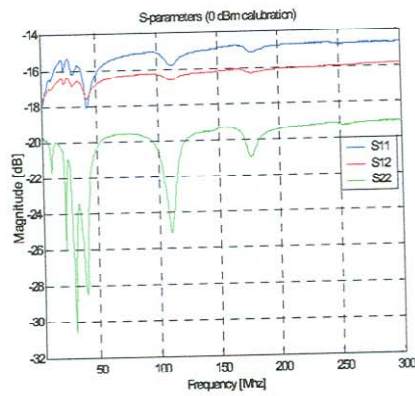


Figure 6.22 : Reverse isolation and impedances of MAR-4SM

The MAR4-SM did not show any saturation (Figure 6.21) for an input power of 0 dBm. This amplifier is also matched to 50 Ω (Figure 6.22) and has a flat transfer between 5-300 MHz with 8 dBs of gain.

6.2.4.3 Final design of receiver

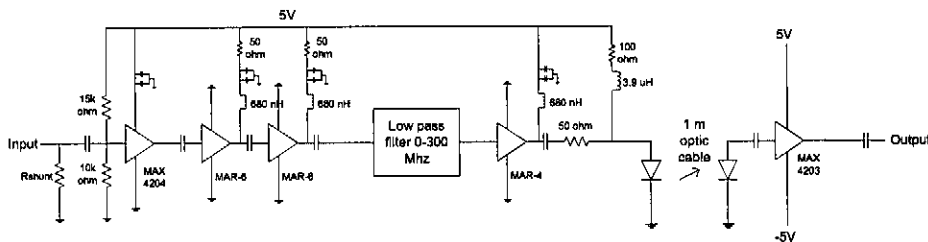


Figure 6.23 : Schematic representation of complete receiver

Figure 6.23 is a schematic representation of the full receiver system, including the optical link. The MAX 4204 input buffer was implemented because it has a 50 Ω output resistance to match the amplifier chain. This resistance will cause additional losses. The buffer was biased at the input, since implementing a negative DC rail was unsuccessful, due to the considerable noise generated by the negative DC-DC converter. The negative DC-DC converter cause pulses on the power line as the flyback capacitor charges and discharges. The shunt resistor at the input was included to shift the receiver between a low input impedance and a high impedance system. A PLP-300 Mini-Circuits low pass filter was included in the receiver chain. The filter has a -3 dB cut-off frequency at 297 MHz (type of filter is unknown).

Since the amplifiers are able to amplify up to 1 GHz, it was necessary to prevent the last stage of the amplifier chain from being driven into saturation due to ambient high frequency noise e.g. from a cell phone band. Figure 6.24 shows the transfer function for the total receiver system as represented by Figure 6.23. Extra gain of a few dBs is achieved due to the open circuit node ($R_{shunt} = \text{open}$) at the input compared to a conventional 50 Ω system ($R_{shunt} = 50 \Omega$). The transfer function has a 4 dB fall between 10-100 MHz that implies a voltage drop over frequency for a 50 Ω system that does not exceed 40%.

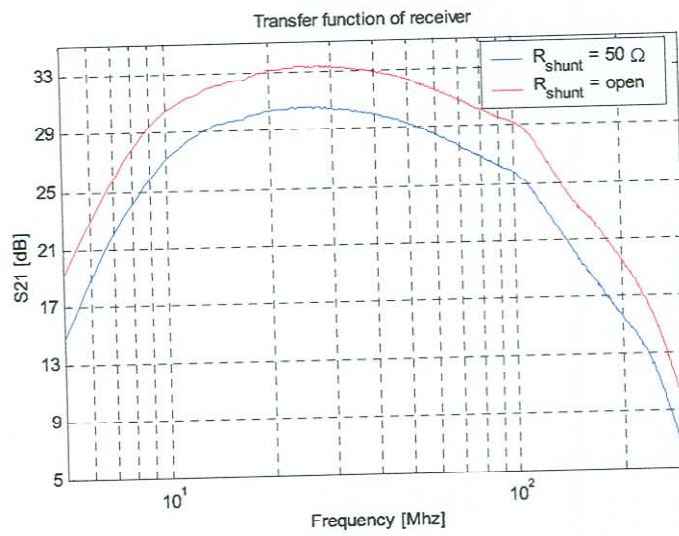


Figure 6.24 : Transfer function of complete receiver

6.2.4.4 Fitting and connectors associated with borehole radar

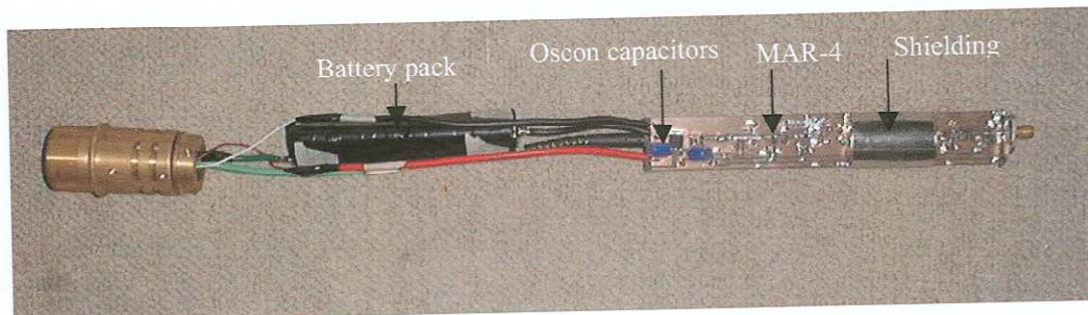


Figure 6.25 : Top view of receiver

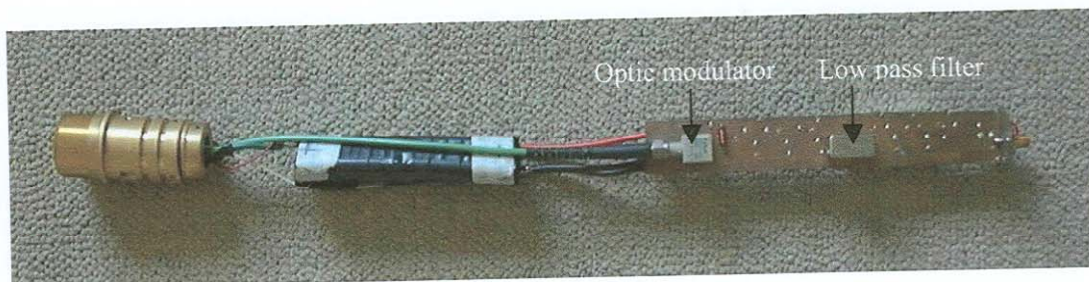


Figure 6.26 : Bottom view of receiver

The MAX 4204 and MAR-4SM are visible in Figure 6.25. The first two gain stages (MAR-6SM) are shielded to prevent coupling and unwanted oscillations. The battery pack consists of six AAA nickel metal hydride cells with a nominal voltage of 1.2 V and nominal capacity of 550 mAh each. Figure 6.26 shows the low pass filter and optic modulator with an SMA connection. Thin (0.5mm) expensive substrate with a permittivity of 2.54 was used to mount the components. The substrate was chosen to prevent surface waves and coupling from the input to output of each amplifier constituting in positive feedback, since the amplifiers are capable of operating in the GHz. The substrate also displays solder markings that represent vias soldered at various sections of the board. The introduction of the electrolytic OSCON capacitors between the DC rails reduced low frequency noise.

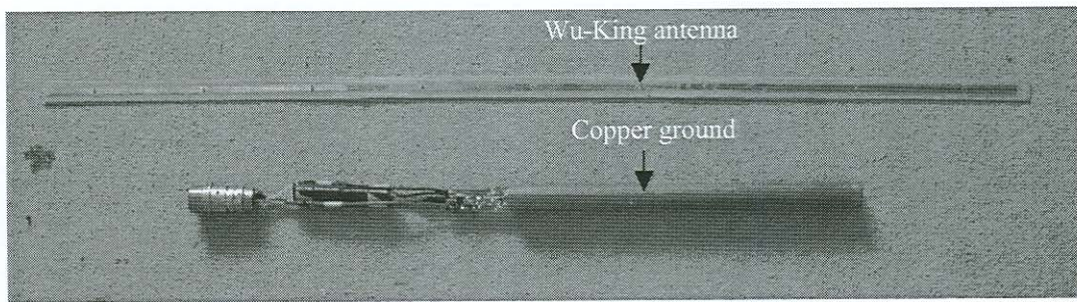


Figure 6.27 : Receiver fitting into copper pipe and 100% Wu-King antenna

Figure 6.27 shows the copper pipe used as ground and housing unit for the electronics and batteries. It also shows the 1m Wu-King antenna designed for air. A brass fitting was machined (Figure 6.28) to house the *LEMO* connector.



Figure 6.28 : Copper housing and LEMO connector.

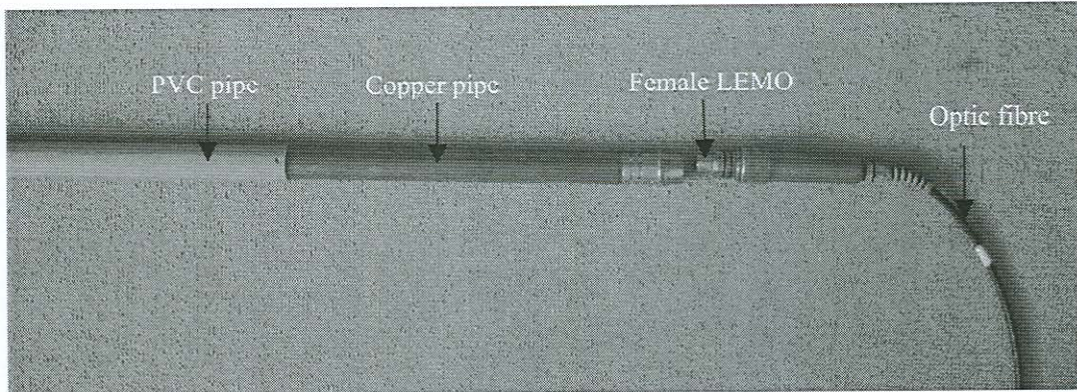


Figure 6.29 : Final assembly of receiver into PVC pipe

The *LEMO* connector provides thru holes in order to connect two optic fibres. It also provide for power connections in order to charge the batteries externally.

Finally the receiver can be fitted into a PVC pipe with an inner diameter of 28mm that will be potted with polyurethane to insulate the electronics against conducting fluids and prevent the probes from being damaged by shock.

6.2.4.5 Impulse response of high impedance receiver

The response of the receiver (Figure 6.23) to a 10ns pulse was investigated in the time domain. A strobe oscilloscope with a $50\ \Omega$ through connection was implemented in order to measure the transient. Figures 6.30 and 6.31 show that the receiver displays a low frequency roll-off with a 50ns period to an input peak pulse of $5.3\ \text{mV}_{\text{peak}}$ and $17\ \text{mV}_{\text{peak}}$. The ratio between first two negative overshoots decrease as the input pulse is increases to $50\ \text{mV}_{\text{peak}}$ (Figure 6.32) that can be attributed to system saturation. The receiver is totally saturated for an input voltage of $170\ \text{mV}_{\text{peak}}$ as the amplitude of the low frequency roll-off starts to increase and the first two absolute peaks are locked. The low frequency ringing in the system may be filtered and the origin of this response should be investigated further. The slow decay may be a function of the filter or of the buffer used, and introduces a long time constant.

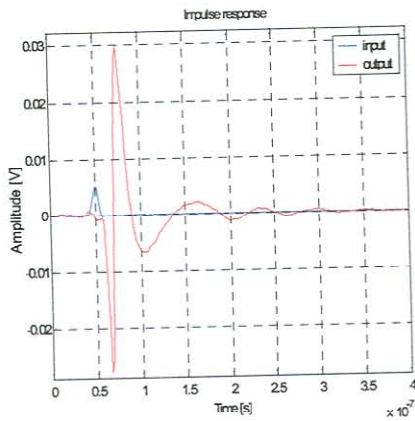


Figure 6.30 : Impulse response to input pulse of 5.3 mV_p

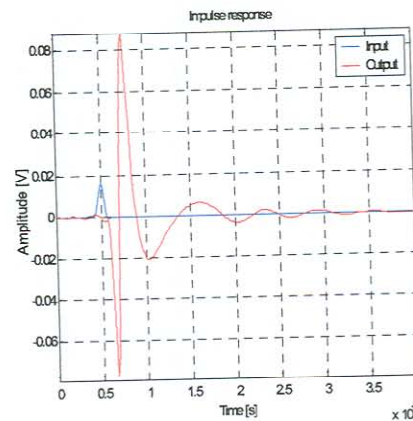


Figure 6.31 : Impulse response to input pulse of 17 mV_p

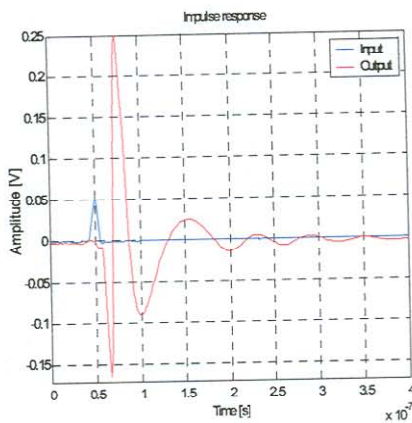


Figure 6.32 : Impulse response to input pulse of 50 mV_p

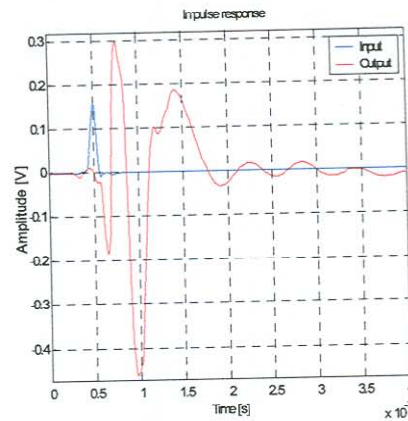


Figure 6.33 : Impulse response to input pulse of 170 mV_p

6.3 Pulse transmitter

For measurement purposes, a pulse transmitter capable of transmitting low voltage signal levels of between 3.5 V and 12 V was used. Figure 6.34 shows the transmitter designed and developed by P. Herselman [21] for calibrating the current radar receivers.

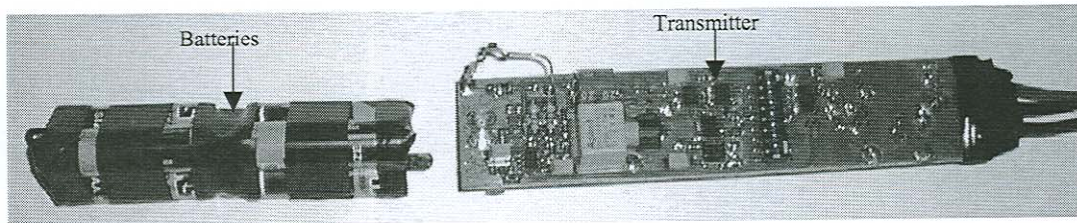


Figure 6.34 : Pulse transmitter used for the measurement of the active antenna

The transmitter is able to transmit $<10\text{ns}$ pulses (frequency content up to 90 MHz), shaped by a push-pull Mosfet output stage. It produces an external reference signal for stacking purposes with an internal monostable clock regulating the pulse repetition frequency of 488 Hz. The transmitter operates from six AAA 1.2 V nickel metal hydride cells.

6.4 Measurements

The test environment (Section 6.4.1) and radar results of the high impedance receiver (Section 6.4.2) are illustrated and discussed in this section.

6.4.1 Measurement and test construction

The radar probes were hoisted up two 110mm underground PVC pipes (Figure 6.34). The pipes provided a combination of strength and light structural weight. The pipes were placed a distance of 6m apart, with a height of 7.5m (Figure 6.35). The indirect wave path is at least 9m longer than the direct wave path that will cause approximately 30 ns separation between the two traces. The important feature of the measurement is that it was constructed in a controlled environment. The optic fibres from the send and receive probes were connected to the optic demodulator and store oscilloscope, as illustrated in Figure 6.36. The optic fibre from the receivers carries the measured signal and the optic fibre from the transmitter carries an external trigger pulse. Semi-rigid $50\ \Omega$ cables and $50\ \Omega$ through connectors were used as electric signal guide between the optic demodulator and oscilloscope (Figure 6.37). A computer running control software for the oscilloscope was implemented to ensure fast storage and stacking of traces.



Figure 6.35 : Structural image of probe test site

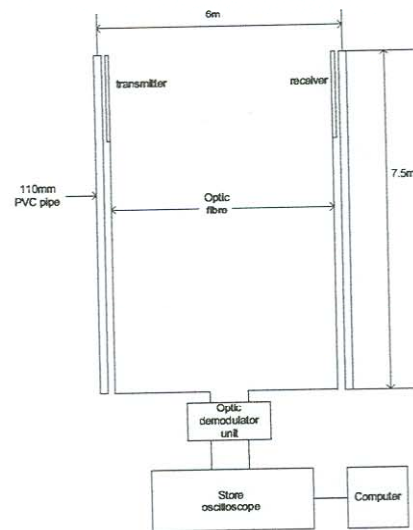


Figure 6.36 : Schematic representation of the implemented measurement testing radar probes

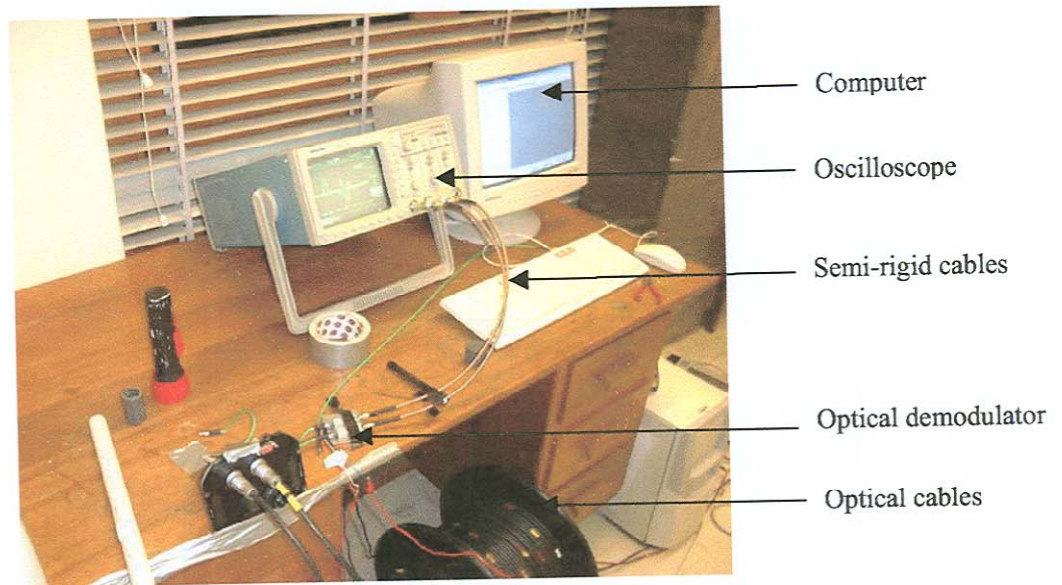


Figure 6.37 : Initialising trace storage equipment

6.4.2 Measurement results

This section discusses the measured external noise levels (Section 6.4.2.1). Stacked time traces from the high impedance receivers and current radar receivers are compared in Section 6.4.2.2 and digital filtering of the desired frequency band is applied to the high impedance trace in section 6.4.2.3.

6.4.2.1 FM external noise

The effect of thermal or white noise was not addressed since adequate signals were transmitted for reception. Stretching the lower limit of the dynamic range was thus not important for the measurement, but will need attention if the system is used in the mine environment. Since the receiver operates in the 10-100 MHz frequency band, it will be susceptible to radio signals. The South African radio band is situated between 88-106MHz. Triggering the receiver without the transmitter trigger pulse reveals the ambient information. Figure 6.38 shows the time traces from the added noise in the radio band. It is important that the high impedance receiver is driven into saturation at certain sections in time. From the impulse response it was clear that the receiver

saturates for output signals above 200 mV. The trigger pulse from the transmitter permits the stacking of the time traces in order to reduce the effect of the FM noise, since the signals will add destructively.

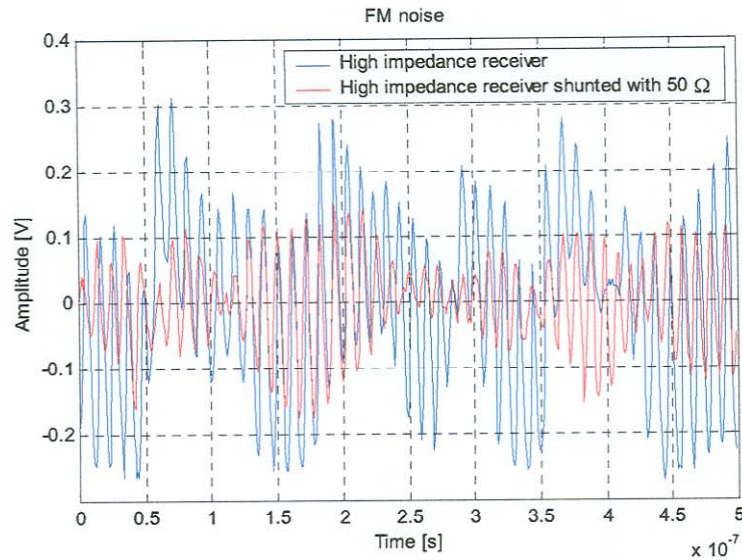


Figure 6.38 : External FM noise measured by receiver

6.4.2.2 Pulse receiving results

Stacking of the received transients was possible up to 30×256 without any pulse degradation. This proves that the transmitter jitter was not severe. The stacking of the signal reduced the FM noise. Figure 6.39 shows the stacked time traces of three receiver systems including the current radar receiver. The high impedance receiver shows an improved pulse waveform with little ringing. The low frequency roll-off is still visible as seen in section 6.2.4.5. The low frequency tail has a long but variable period and filtering the low frequencies may resolve this problem. Both the current radar and a 50Ω shunted high impedance receiver display the same ringing behaviour in their time traces. The previous section showed that the external noise constantly saturated the high impedance receiver. This may have some effect on the measured result. The *Fast Fourier Transform* (Figure 6.40) of the time traces was implemented over a time window of 500 ns with 500 samples. The flat response of the high impedance receiver closely resembles simulated

results. A spike is visible in the frequency response below 90 MHz and proves that there are reflections in the data because it is visible for both the high impedance receiver and current receiver. It is difficult to determine the effect of the reflection on the time trace.

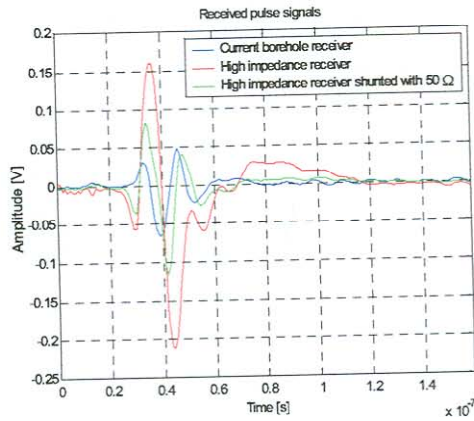


Figure 6.39 : Receiver time trace

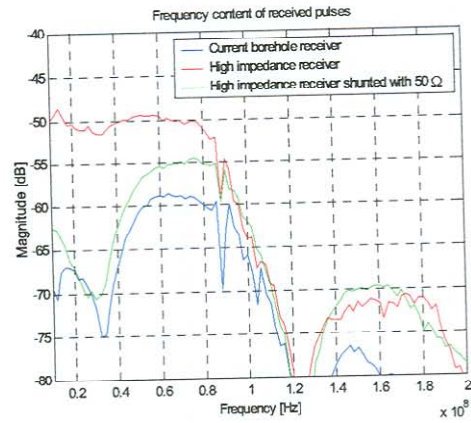
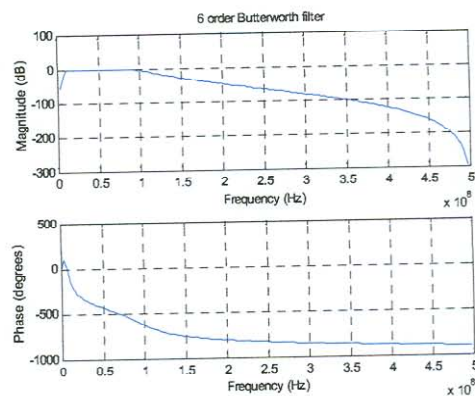


Figure 6.40 : Frequency response of received pulse

6.4.2.3 Digital filtering

Digital filtering of the desired frequency band was applied to the high impedance receiver trace to test whether the low frequency roll-off can be eliminated from the time trace. A 6th order Butterworth filter (Figure 6.41) was applied in the time domain. The choice of the Butterworth filter was supplemented by its linear phase properties at the cut-off frequencies.

Figure 6.41 : Frequency response of 6th order Butterworth filter

By applying forward and reverse digital filtering it is possible to eliminate the influence of the filter phase and the choice of the filter is not that important. The filtered time trace displays a definite low frequency component in the desired band that is situated in the slow decaying tail (Figure 6.42). The period of the oscillating tail represents a frequency component around 13 MHz. The high, low frequency energy visible in the frequency response (Figure 6.43) causes some dispersion in the time trace due to their slow decay.

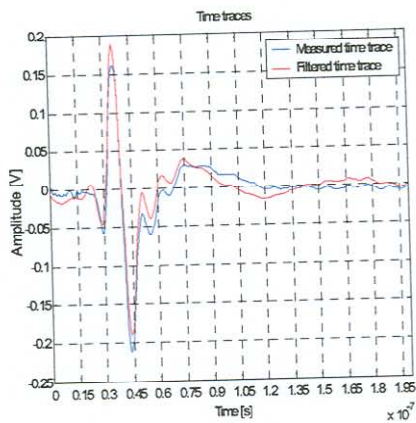


Figure 6.42 : Original and filtered measured time trace of high impedance receiver

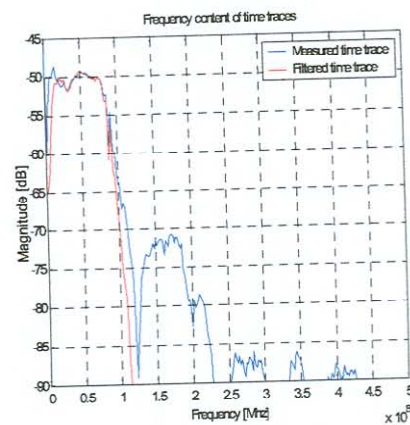


Figure 6.43 : Frequency response of original and filtered time trace of high impedance receiver

6.5 Conclusion

The low frequency roll-off of the high impedance receiver seems acceptable when the system does not saturate and the transient dies off in the pulse repetition frequency time window. Further testing of the system should be conducted in a mine environment in order to fully determine whether the system has an advantage above the conventional 50Ω receiver.

From *Chapter 5* it is evident that the efficiency of the antenna improves when the dielectric constant of the ambient increases, which will increase the power received by the 50Ω receiver. The resonance occurring in the desired frequency band (above 50 MHz) for the antenna dimensions simulated in rock in *Chapter 5*, may cause unfavourable conditions for the effective use of a high impedance receiver. The resonance will cause ringing and the antenna length

(primarily the ground arm) should be reduced to limit the resonance above 100 MHz, even for the 50 Ω system. The most important feature of the active antenna is that it reacts like an electric field probe.

Chapter 7

CONCLUSIONS

7.1 Conclusions

Modelling and characterization of a wire radiating structure suitable for fitting into a borehole for pulse ground penetration radar applications was presented. The results will be presented, following the thesis outline.

7.1.1 Verification of simulation tools

- Two commercial numerical simulation packages, namely FEKO™ and CST™ were verified as being accurate means for simulating resistively and insulated antennas in the borehole environment.
- Numerical modelling helps to understand the electromagnetic behaviour of radiating structures in different environments without resorting to physical measurement techniques.

7.1.2 Investigating time-domain radiation for wire antennas

- The travelling wave elements give physical insight into the transient radiation of conducting wire antennas not readily available from the time-harmonic analysis. Radiation is connected to the reflection of a charge.
- An electrically small dipole antenna produces an oscillating theta electric field that is linked to a natural frequency, which is a function of the physical dimension of the antenna.

- Different radiation mechanisms are observed when a conducting dipole antenna is excited by a voltage or current source that influence the oscillating electric field produced by the antenna.

7.1.3 Theoretical and numerical modelling of insulated antennas

- The *TLM* was verified with FEKO™ and produced adequate results as a modelling tool for both conducting and resistively loaded wire antennas in a borehole surrounded by rock.
- The model is not applicable to bare antennas in a medium and electrically long wire antennas.
- It was also shown, by using a mathematical representation of the combined air insulation of the borehole and antenna insulation, that the air layer has a dominating influence on the antenna.

7.1.4 Modelling of radar probes

- The asymmetric resistively loaded antenna presented by D. M. Claassen [3] may be the most practical structure for pulse radiation in the borehole environment. It displays small variations in its input impedance for dielectric and conductive changes associated with rock.
- The resistive arm shifts the first resonance of a conducting dipole up in frequency. The short resistive arm of the current radar technology was chosen to suppress the first resonance, as well as to shift it above the frequency band of interest. As showed by D. M. Claassen [3], the ground arm determines the basic frequency operation of the asymmetric resistively loaded dipole.
- Physical implementation of a symmetrical resistively loaded antenna is difficult, due to the amount of space required for the electronic equipment.
- For frequencies of 70-90 MHz the antenna pattern squints towards the resistive arm and for frequencies above 150 MHz the pattern squints towards the ground arm (concerning the asymmetrical dipole for the dimensions used in these simulations).
- The asymmetric antenna has been shown to be adequate as a pulse radiator since its pattern is stable over the desired frequency band and does not produce multiple lobes.

- A 50% Wu-King resistive loading adds little ringing to the transmitted electric field time transient of the asymmetric dipole for better signal levels when compared to the conventional 100% Wu-King loading.
- Symmetrical Wu-King resistive loading provides a constant natural frequency in the transmitted electric field, even for lower percentage resistor values. Center and source loading may also be considered, since the electrically small antenna struggles to launch a travelling wave.
- It was not feasible to extract the electric field trace at a distance from an insulated antenna in CST™, due to the small meshing required to simulate the borehole near the antenna, which in turn produces a computer-intensive simulation.
- It became apparent that an electrically small resistively loaded antenna could be used as a wideband electric field receiving probe if a high source load is used.

7.1.5 Active receiving antenna

- The optical link carrying the trigger and received signal from the radar up the borehole was re-examined. A possible solution that reduces the components needed to drive the optical modulator and which results in a flatter transfer function than the current radar system was presented.
- An active antenna incorporating a 100% Wu-King resistively loaded antenna and a conducting ground arm was built and tested. Optimistic results were obtained which verified the simulated results when used as a receiving antenna.
- The active antenna is an electric field probe and produces a higher resolution pulse but has an undesirable low frequency roll-off. The antenna makes use of the capacitive nature of the input impedance and produces a flat transfer function and improved sensitivity.

7.2 Future work

The ground arm can be loaded by using ferrite rings to make a symmetrical radiator. The active antenna should be tested in a mine environment to determine its practicality and to test whether the antenna's dynamic behaviour does not start to play a negative role. The full dynamic range

and noise considerations of the system and front-end current feedback amplifier should be investigated.

The low frequency roll-off may cause degradation of the received pulse if the recovery period of the receive electronics does not occur fast enough after being illuminated by the direct transmit pulse.

Chapter 8

REFERENCES

- [1] M. D. van Wyk, Kopanang mine, South Africa, December 2000.
- [2] J. Hargreaves, *A Multichannel Borehole Radar for Three Dimensional Imaging*, PhD thesis, University of Oxford, trinity term 1995.
- [3] D. M. Claassen, *Electromagnetic characterization of wideband borehole radar imaging system*, PhD thesis, University of Oxford, Trinity term 1995.
- [4] W. L. Stutzman and G. A. Thiele, *Antenna Theory and Design*, John Wiley & Sons, Inc., 2nd Edition, 1998.
- [5] T. T. Wu and R. W. P. King, "The cylindrical antenna with non-reflecting resistive loading", *IEEE Transactions Antennas and Propagation*, vol. AP-13, pp. 369-373, May 1965.
- [6] C. M. Butler, "The equivalent radius of a narrow conducting strip", *IEEE Transactions Antennas and Propagation*, vol. AP-30, pp. 755-757, July 1982
- [7] S. Keller, *Design of Impedance Loaded Antennas for Broadband Radar Applications*, Diploma thesis, University of Stellenbosch, Stellenbosch, South Africa, July 2000.
- [8] B. D. Popovic, *CAD of Wire Antennas and related Radiating Structures*, New York, Research Studies Press, 1991.
- [9] A. von Hippel, *Dielectric Materials and Applications*, The MIT press, 3rd Edition, 1954.
- [10] L. Hartshorn and W. H. Ward, "The measurement of the permittivity and power factor of dielectrics at frequencies from 10^4 to 10^8 cycles per second", *Nat. Physics*, pp 597-609, July 1936.
- [11] G. S. Smith, "Teaching antenna radiation from a time-domain perspective", *Am. J. Phys*, vol. 69, pp. 288-300, March. 2001.
- [12] E. K. Miller, "A Multi-perspective examination of Electromagnetic Radiation", Personal communication, E. K. Miller with J. H. Cloete, Maart 2001.
- [13] S. A. Schelkunoff, "Theory of Antennas of Arbitrary Size and Shape", *Proc. of the I. R. E.*, pp. 493-521, Sept. 1941.
- [14] R. W. P. King, G. S. Smith, T. T. Wu, and M. Owens, *Antennas in Matter*, The MIT

- Press, 1981.
- [15] K. C. Chen and L. K. Warne, "A Uniformly Valid Loaded Antenna Theory", *IEEE Transactions Antennas and Propagation*, vol. AP-40, pp. 1313-1323, Nov. 1992.
 - [16] R. W. P. King, B. S. Trembly, J. W. Strohbehm, "The Electromagnetic Field of an Insulated Antenna in a Conducting or Dielectric Medium", *IEEE Transactions on Microwave Theory and Techniques*, vol. MTT-31, pp. 575-583, July 1983.
 - [17] Marc Röchlin, Personal communication, August 2001.
 - [18] T. P. Montoya and G. S. Smith, "A Study of Pulse Radiation from Several Broad-Band Loaded Monopoles", *IEEE Transactions Antennas and Propagation*, vol. AP-44, pp.1172-1182, August 1996.
 - [19] K. P. Esselle and S. S. Stuchly, "Pulse-Receiving Characteristics of Resistively Loaded Dipole Antennas", *IEEE Transactions Antennas and Propagation*, vol. AP-38, pp. 1677-1683, Oct. 1990.
 - [20] Low Cost, Miniature Fiber Optic Components with ST[®], SMA, SC and FC Ports, Technical data, Agilent Technologies™.
 - [21] P. Le R. Herselman, Personal communication, November 2001.

APPENDIX A1

The theoretical derivation of the Wu-King Profile

The following is based on an appendix by S. Keller [5]. It is shown that, by adding a certain variable impedance per unit length, an axial current distribution which consists of a pure outward travelling wave can be obtained for a dipole antenna. The vector potential $A_z(z)$ on the surface of a cylindrical antenna that has the internal impedance per unit length $z^i(z)$, carries a total current $I_z(z)$ and is driven at $z=0$ by a delta-function generator with emf V_0 satisfies the one-dimensional equation in the form

$$\left(\frac{\partial^2}{\partial z^2} + k_0^2 \right) A_z(z) = \frac{jk_0^2}{\omega} [z^i(z)I_z(z) - V_0\delta(z)] \quad (\text{A.1})$$

if a time-dependence $e^{j\omega t}$ is assumed. The internal impedance per unit length $z^i(z)$ is expressed as a function of the axial coordinate z by

$$z^i(z) = \frac{1}{2\pi a d(z)\sigma(z)} \quad (\text{A.2})$$

for a circular tube with constant radius a . The impedance per unit length can either be varied by a variable wall thickness $d(z)$ or a variable conductivity $\sigma(z)$. The vector potential on the surface of the antenna is

$$A_z(z) = \frac{\mu_0}{4\pi} \int_{-h}^h I_z(z')K(z, z')dz' \quad (\text{A.3})$$

where $K(z, z') = \frac{e^{-jk_0 r}}{r}$ with $r = \sqrt{(z - z')^2 + a^2}$

The ratio of vector potential to current along an antenna is approximately constant, making it possible to set

$$\int_{-h}^h I_z(z)K(z, z')dz' = I_z\psi \quad (\text{A.4})$$

where ψ is the magnitude where the current has a maximum. Using equation (A.4) and setting the intrinsic impedance equal to $\zeta_0 = \sqrt{\mu_0/\epsilon_0} = 120\pi \Omega$ and the notation,

$$f(z) = \frac{4\pi}{\zeta_0\psi} z^i(z) \quad (\text{A.5})$$

equation (A.1) can be approximated by

$$\left[\frac{\partial^2}{\partial z^2} + k_o^2 - jk_o f(z) \right] I_z(z) = -\frac{j4\pi k_o}{\zeta_o \psi} V_o \delta(z) \quad (\text{A.6})$$

The currents must satisfy the differential equation

$$\left[\frac{\partial^2}{\partial z^2} + k_o^2 - jk_o f(z) \right] I_z(z) = 0 \quad (\text{A.7})$$

except at the driving point $z = 0$. By direct substitution in (A.7) it can be shown that, if

$$f(z) = \frac{2}{h - |z|} \quad (\text{A.8})$$

a solution of (1.7) is:

$$I_z(z) = C(h - |z|)e^{-jk_o|z|} \quad (\text{A.9})$$

The solution, equation (A.9), represents a wave of current travelling in the direction of increasing $|z|$, which is from the generator to the open ends of the antenna. There is no reflected wave travelling in the opposite direction. The constant C in equation (A.9) can be determined by using the Lorenz condition:

$$\Phi(z) = \frac{j\omega}{k_o^2} \frac{\partial A_z(z)}{\partial z} \quad (\text{A.10})$$

together with

$$A_z(z) = \frac{\mu_o}{4\pi} \psi C(1 + jk_o h)e^{-jk_o|z|} \quad (\text{A.11})$$

Assuming the symmetry $\Phi(-z) = -\Phi(z)$ for $z \geq 0$ and that the driving voltage is defined by

$$V_o = \Phi(+0) - \Phi(-0) = 2\Phi(0) \quad (\text{A.12})$$

it follows that

$$C = \frac{j2\pi\omega\epsilon_o V_o}{\psi(1 + jk_o h)} \quad (\text{A.13})$$

Therefore the current distribution is finally defined by

$$I(z) = \frac{2\pi V_o}{\zeta_o \Psi \left(1 - \frac{j}{k_o h}\right)} \left(1 - \frac{|z|}{h}\right) e^{-jk_o|z|} \quad (\text{A.14})$$

The continuous resistive loading profile, which is needed to obtain this travelling wave current distribution is defined by (A.5) together with (A.8), thus,

$$Z^i(z) = \frac{\zeta_o \Psi}{2\pi} \frac{1}{h - |z|} = \frac{60\Psi}{h - |z|} \quad (\text{A.15})$$

where the coefficient 60 is in ohms.

The expansion parameter represents the ratio of the vector potential $A_z(z)$ to the current $I_z(z)$ at the driving point. It depends on the total length of the dipole, $2h$, the radius of the dipole, a , and

the design frequency, represented by the wave number $k_0=2\pi f/c_0$. The following approximation was given, which is valid, since $k_0 a \ll 1$ and $a \ll h$.

$$\Psi = 2 \left[\sinh^{-1} \left(\frac{h}{a} \right) - C(2k_0 a, 2k_0 h) - jS(2k_0 a, 2k_0 h) \right] + \frac{j}{k_0 h} [1 - e^{-j2k_0 h}] \quad (\text{A.16})$$

where C and S are the generalized sine and cosine integrals given by

$$S(b, x) = \int_0^x \frac{\sin W}{W} du$$

$$C(b, x) = \int_0^x \frac{1 - \cos W}{W} du$$

where $W = \sqrt{u^2 + b^2}$

APPENDIX A2

Theory of an RC circuit for measurement of a dielectric specimen

The theory in this section is based on Von Hippel [9]. A capacitor, connected to a sinusoidal voltage source,

$$\bar{V} = V_o e^{j\omega t} \quad (\text{A.1})$$

of the angular frequency,

$$\omega = 2\pi f \quad (\text{A.2})$$

stores, when its dielectric is a vacuum, a charge,

$$Q = C_o \bar{V} \quad (\text{A.3})$$

and draws a charge current,

$$I_c = \frac{dQ}{dt} = j\omega C_o \bar{V} \quad (\text{A.4})$$

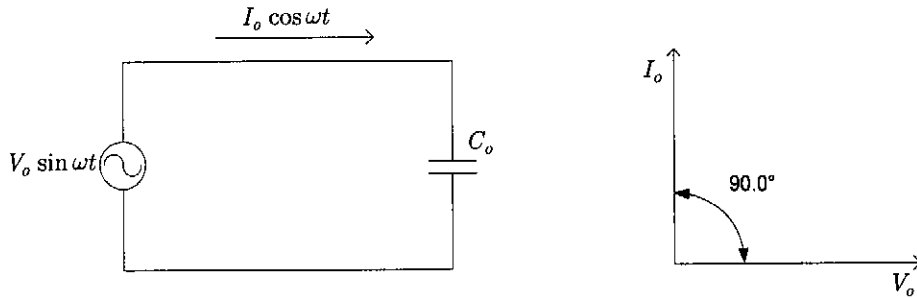


Figure A2-1 : Current voltage relationship in ideal capacitor

leading the voltage by a temporal phase angle of 90° (Figure A2-1). C_o is the vacuum capacitance of the condenser. When filled with some substance, the condenser increases its capacitance to

$$C = C_o \frac{\epsilon'}{\epsilon_o} = C_o \kappa' \quad (\text{A.5})$$

where ϵ' and ϵ_o designate the real permittivities or dielectric constants of the dielectric and of the vacuum, respectively, and the ratio κ' the relative dielectric constant of the material. Simultaneously, there may appear, in addition to the charging current component I_c , a loss current component

$$I_l = G\bar{V} \quad (\text{A.6})$$

in phase with the voltage; G represents the conductance of the dielectric. The total current traversing the condenser,

$$I = I_c + I_l = (j\omega C + G)\bar{V} \quad (\text{A.7})$$

is inclined by a power factor angle $\theta < 90^\circ$ against the applied voltage \bar{V} , that is, by a loss angle δ against the $+j$ -axis (Figure A2-2).

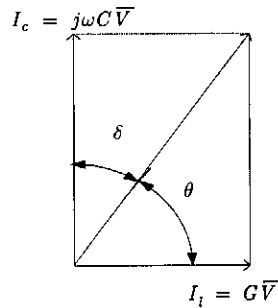


Figure A2-2 : Capacitor containing dielectric with loss

The ratio of the loss current to the charging current gives the dissipation factor D given by,

$$D = \tan \delta = \frac{I_l}{I_c} = \frac{1}{\omega RC} \quad (\text{A.8})$$

APPENDIX A3

Theory of resonating RLC circuit for measurement of a dielectric specimen

The section is based on a paper presented by Hartshorn and Ward [10]. The Marconi dielectric meter uses the susceptance-variation method that makes use of the fact that the shape, in particular the width, of a resonance curve of a resonant circuit is a measure of the dissipation factor of the circuit.

The Marconi circuit magnification meter can be reduced to its essential elements as shown diagrammatically in Figure A3.1. A sample of dielectric to be tested is placed between the two metal plates (Series Loss Test Jig TJ 230), thereby forming a condenser of capacitance C_1 , to which a coil L , R , and a thermionic voltmeter V is connected.

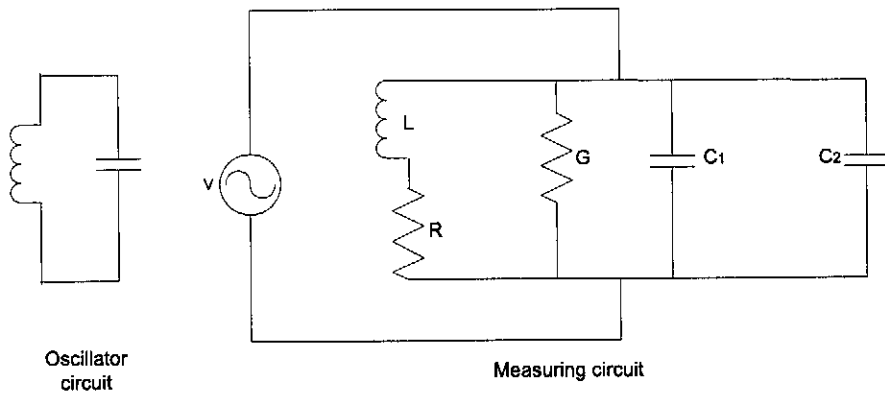


Figure A3-1: Equivalent circuit diagram of Marconi magnification meter

A second condenser C_2 is connected in parallel with these components and the oscillatory circuit. Regard the circuit as divided into two parts : (a) the coil system, which includes all the inductive portions of the circuit together with its distributed capacitance; and (b) the part external to the coil, namely C_1 , C_2 and V . The voltmeter indicates,

$$V = \frac{I}{G + jC\omega} = \frac{V_\infty}{(R + jL\omega)(G + jC\omega) + 1}$$

or

$$V = \frac{V_\infty}{R + jL\omega} \frac{1}{G + \frac{R}{Z^2} + j\omega(C - \frac{L}{Z^2})}$$

(A.1)

where $Z^2 = R^2 + L^2\omega^2$

If the capacitance C is varied, the other quantities remaining constant, then the only term in this expression which varies is $j\omega(C-L/Z^2)$ and it is obvious that the voltage V will reach a maximum value when

$$C = \frac{L}{Z^2} = C_r \quad (\text{A.2})$$

C_r is therefore the value of the total capacitance corresponding to voltage resonance. The ratio of the voltage V at any other value of capacitance C to the value V_r at resonance is given by

$$\frac{V_r^2}{V^2} = \frac{(G + \frac{R}{Z^2})^2 + \omega^2(C - \frac{L}{Z^2})^2}{(G + \frac{R}{Z^2})^2} \quad (\text{A.3})$$

Thus the capacitance C corresponding to any given value of $q = V_r^2/V^2$ is given by

$$C = \frac{L}{Z^2} \pm \frac{(G + \frac{R}{Z^2})\sqrt{q-1}}{\omega} \quad (\text{A.4})$$

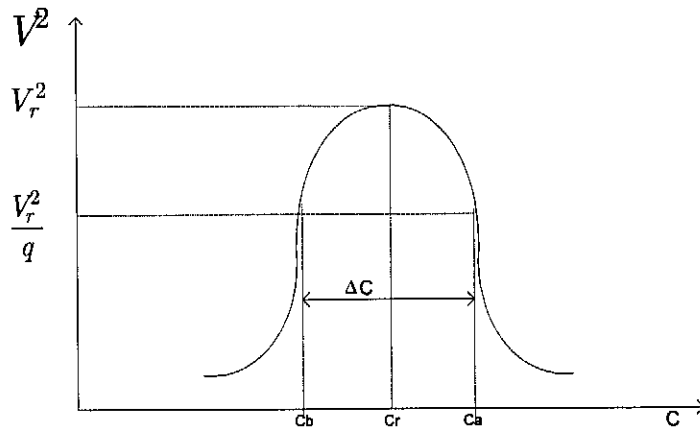


Figure A3-2 : Resonance curve

Now R/Z^2 is the equivalent shunt conductance of the coil, so that $G + \frac{R}{Z^2}$ is the total equivalent conductance G_t of the whole circuit. Thus the equation becomes

$$C = C_r \pm \frac{G_t\sqrt{q-1}}{\omega} \quad (\text{A.5})$$

If, therefore, we denote by C_a and C_b the two values of C (one on either side of the resonance curve) and Figure A3.2 giving any particular value of V , we have, by taking the sum and difference of equations (A.5)

$$C_r = \frac{1}{2}(C_a + C_b)$$

and

$$(A.6)$$

$$G_i = \frac{\omega(C_a - C_b)}{2\sqrt{q-1}} = \frac{\omega\Delta C}{2\sqrt{q-1}}$$

The resonance curve is symmetrical, which makes equation (A.6) correct. In order to determine the properties of the sample of insulating material apart from those of the remainder of the circuit, two series of observations are necessary. The first consists of observations of C_r , θ_r , ΔC , and q . The sample is next removed from its position between the metal plates, which are then brought nearer together until resonance is again established with air as insulation. Evidently the total capacitance in the second case (air) must be exactly the same as that in the first, since equation (A.2) for the capacitance at resonance is completely independent of the conductance G , which is the only factor that has been changed. The differences between the conductance G and G_i with and without the sample, is the conductance G_s of the sample. G_s is given by

$$G_s = \frac{\omega(\Delta C_i - \Delta C_o)}{2\sqrt{q-1}} \quad (A.7)$$

where ΔC_i = Difference in capacitance with sample

ΔC_o = Difference in capacitance without sample

The value of the air-capacitance C_{air} in the second case (sample out), which may readily be calculated from the dimensions of the plates and their distance apart, is evidently equal to the capacitance C_s of the sample. The loss tangent is given by,

$$\tan \delta = \frac{G_s}{C_s \omega} = \frac{(\Delta C_i - \Delta C_o)}{2C_s \sqrt{q-1}} \quad (A.8)$$

APPENDIX B1

Charge per unit length on the basic travelling-wave element

The equation of continuity for electric charge in one special dimension,

$$\frac{\partial I(z,t)}{\partial z} = -\frac{\partial Q(z,t)}{\partial t}, \quad (\text{B.1})$$

can be integrated to give

$$Q(z,t) = -\int_{t'=-\infty}^t \frac{\partial I(z,t')}{\partial z} dt', \quad (\text{B.2})$$

where it is assumed that $Q(z,t = -\infty) = 0$. On substitution of the distribution of current it becomes

$$\begin{aligned} Q(z,t) &= -\int_{t'=-\infty}^t \frac{\partial I_s(t' - z/c)}{\partial z} dt' [U(z) - U(z-h)] \\ &\quad - \int_{t'=-\infty}^t I_s(t' - z/c) dt' \frac{\partial}{\partial z} [U(z) - U(z-h)] \\ &= -\int_{t'=-\infty}^t \frac{\partial I_s(t' - z/c)}{\partial z} dt' [U(z) - U(z-h)] \\ &\quad - \int_{t'=-\infty}^t I_s(t') dt' \delta(z) \\ &\quad + \int_{t'=-\infty}^t I_s(t' - h/c) dt' \delta(z-h) \end{aligned} \quad (\text{B.3})$$

Now the relation

$$\frac{\partial I_s(t - z/c)}{\partial z} = -\frac{1}{c} \frac{\partial I_s(t - z/c)}{\partial t} \quad (\text{B.4})$$

can be used to evaluate the first integral and obtain the final expression for the charge per unit length:

$$\begin{aligned} Q(z,t) &= \frac{1}{c} I_s(t - z/c) [U(z) - U(z-h)] \\ &\quad - \int_{t'=-\infty}^t I_s(t') dt' \delta(z) + \int_{t'=-\infty}^t I_s(t' - h/c) \\ &\quad \times dt' \delta(z-h), \end{aligned} \quad (\text{B.5})$$

where it is assumed that $I_s(z,t = -\infty) = 0$.

APPENDIX B2

Electromagnetic field of the basic travelling-wave element

The scalar electric potential Φ and the vector magnetic potential A in the Lorentz gauge are given by the following integrals of the volume charge density ρ and the volume current density J :

$$\Phi(r, t) = \frac{1}{\epsilon_0} \int_{t'=-\infty}^{\infty} \iiint_V \rho(r', t') \times G_o(r, r'; t, t') dV' dt', \quad (\text{B.1})$$

$$A(r, t) = \mu_0 \int_{t'=-\infty}^{\infty} \iiint_V J(r', t') \times G_o(r, r'; t, t') dV' dt', \quad (\text{B.2})$$

where r' locates the source point, r locates the field point, and G_o is the free-space, scalar Green's function:

$$G_o(r, r'; t, t') = \frac{\delta(t - t' - R/c)}{4\pi R}, \quad R = |r - r'| \quad (\text{B.3})$$

For the basic travelling-wave element, the charge and current are confined to the z axis, and there is only one component to the current (z); hence (B.1) and (B.2) simplify to become

$$\Phi(r, t) = \frac{1}{\epsilon_0} \int_{t'=-\infty}^{\infty} \int_{z'=-\infty}^{\infty} Q(z', t') \times G_o(r, z'; t, t') dz' dt', \quad (\text{B.4})$$

$$A_z(r, t) = \mu_0 \int_{t'=-\infty}^{\infty} \int_{z'=-\infty}^{\infty} I(z', t') \times G_o(r, z'; t, t') dz' dt', \quad (\text{B.5})$$

with

$$G_o(r, z'; t, t') = \frac{\delta(t - t' - R/c)}{4\pi R}, \quad R = \sqrt{x^2 + y^2 + (z - z')^2} \quad (\text{B.6})$$

After inserting the charge into (B.4) and the current into (B.5), using the properties of the step and delta functions, and introducing the change of variable,

$$\eta = t - R/c - z'/c, \quad d\eta = \frac{\eta + z'/c - t}{R} dz', \quad (\text{B.7})$$

$$\Phi(r, t) = \frac{1}{4\pi\epsilon_0} \left[\frac{1}{r} q_o(t - r/c) + \frac{1}{r_h} q_h(t - r_h/c) + \int_{\eta=t-r/c}^{t-r_h/c} \frac{Q(\eta)}{\eta + z'/c - t} d\eta \right], \quad (\text{B.8})$$

$$A_z(r, t) = \frac{\mu_0}{4\pi} \int_{\eta=t-r/c}^{t-h/c-r_h/c} \frac{I_s(\eta)}{\eta + z/c - t} d\eta. \quad (\text{B.9})$$

Now the potential functions must be differentiated to obtain the electric and magnetic fields:

$$E = -\nabla\Phi - \frac{\partial A_z}{\partial t} \hat{z}, \quad (\text{B.10})$$

$$B = \nabla \times (A_z \hat{z}) = -\hat{z} \times \nabla A_z. \quad (\text{B.11})$$

After inserting (B.8) and (B.9) into (B.10) and (B.11) and using Leibniz's rule to differentiate the integrals, the electric and magnetic fields become

$$\begin{aligned} E(r, t) = & -\frac{1}{4\pi\epsilon_0} \left\{ \nabla \left[\frac{q_0(t-r/c)}{r} \right] + \nabla_h \left[\frac{q_h(t-r_h/c)}{r_h} \right] \right. \\ & - \left[\frac{I_s(t-r/c)}{z-r} \right] \nabla(t-r/c) \\ & + \left[\frac{I_s(t-h/c-r_h/c)}{(z-h)-r_h} \right] \nabla_h(t-h/c-r_h/c) \\ & + \int_{\eta=t-r/c}^{t-h/c-r_h/c} \frac{1}{c} I_s(\eta) \nabla \left(\frac{1}{\eta + z/c - t} \right) d\eta \\ & - \frac{1}{c} \left[\frac{I_s(t-r/c)}{z-r} - \frac{I_s(t-h/c-r_h/c)}{(z-h)-r_h} \right. \\ & \left. - \int_{\eta=t-r/c}^{t-h/c-r_h/c} \frac{1}{c} I_s(\eta) \frac{\partial}{\partial t} \left(\frac{1}{\eta + z/c - t} \right) d\eta \right] \hat{z} \}, \end{aligned} \quad (\text{B.12})$$

$$\begin{aligned} B(r, t) = & \hat{z} \times \left(\frac{\mu_0}{4\pi} \left\{ c \left[\frac{I_s(t-r/c)}{z-r} \right] \nabla(t-r/c) \right. \right. \\ & - c \left[\frac{I_s(t-h/c-r_h/c)}{(z-h)-r_h} \right] \nabla_h(t-h/c-r_h/c) \\ & \left. \left. - \int_{\eta=t-r/c}^{t-h/c-r_h/c} I_s(\eta) \nabla \left(\frac{1}{\eta + z/c - t} \right) d\eta \right\} \right). \end{aligned} \quad (\text{B.13})$$

It is permissible to perform the gradient and curl operation in (B.10) and (B.11). The final expressions for the electric and magnetic fields are obtained by performing the differentiations in (B.12) and (B.13) and combining terms

$$\begin{aligned} E(r, t) = & \frac{1}{4\pi\epsilon_0} \left[\frac{q_0(t-r/c)}{r^2} \hat{r} + \frac{q_h(t-r_h/c)}{r_h^2} \right. \\ & + \frac{\cot(\theta/2) I_s(t-r/c)}{cr} \hat{\theta} \\ & \left. - \frac{\cot(\theta_h/2) I_s(t-h/c-r_h/c)}{cr_h} \hat{\theta}_h \right], \end{aligned} \quad (\text{B.14})$$

$$B(r, t) = \frac{\mu_0}{4\pi} \left[\frac{\cot(\theta/2) I_s(t - r/c)}{r} - \frac{\cot(\theta_h/2) I_s(t - h/c - r_h/c)}{r_h} \right] \hat{\phi}. \quad (\text{B.15})$$

APPENDIX B3

The Discrete Fourier Transform for aperiodic finite-energy sequences

Aperiodic finite-energy signals have continuous spectra. Consider an aperiodic discrete-time signal $x(n)$ with a Fourier transform,

$$X(\omega) = \sum_{n=-\infty}^{\infty} x(n)e^{-j\omega n} \quad (\text{B.1})$$

Since $X(\omega)$ is periodic with period 2π , only samples in the fundamental frequency ($\omega = 2\pi k / N$) range are necessary. The reconstructed signal,

$$x_p(n) = \sum_{l=-\infty}^{\infty} x(n - lN) \quad (\text{B.2})$$

is obtained by the periodic repetition of $x(n)$ every N samples. Consequently, it can be expanded in a Fourier series as

$$x_p(n) = \sum_{k=0}^{N-1} c_k e^{j2\pi kn/N} \quad n = 0, 1, \dots, N-1 \quad (\text{B.3})$$

with Fourier coefficients

$$c_k = \frac{1}{N} \sum_{n=0}^{N-1} x_p(n) e^{-j2\pi kn/N} \quad k = 0, 1, \dots, N-1 \quad (\text{B.4})$$

Therefore,

$$x_p(n) = \frac{1}{N} \sum_{k=0}^{N-1} X\left(\frac{2\pi k}{N}\right) e^{j2\pi kn/N} \quad n = 0, 1, \dots, N-1 \quad (\text{B.5})$$

The $1/N$ normalization factor is derived by Parseval's theorem to keep the energy in both the time domain and frequency domain equal. $X(\omega)$ can be constructed from the periodic signal $x_p(n)$ if there is no aliasing. All signals in this work had a repetition period of 500ns with 11760 samples. The *Discrete Fourier Transform* is a representation of the energy at each frequency for a given time signal. Transmission functions obtained thus represent the energy coupling between a given input and output. If for example the upper saturation limit of a given receiver needs to be calculated, the magnitude plot does not give sufficient information about the physical real limit of the received signal. If the magnitude of a certain frequency displays better energy coupling than another it may not set the upper limit of the real physical input signal. It depends on the period of time the energy is distributed.

APPENDIX C1

Derivation of the input impedance of a variable two-section insulated dipole antenna

The setup of Figure 4.9 in *Chapter 4* is used in this appendix. The telegrapher equations for a transmission line with distributed series impedance z per unit length and distributed admittance y per unit length are

$$\begin{aligned}\frac{dV_i(z)}{dz} &= -z_i I_i, -h \leq z < 0, i = 1 \\ \frac{dI_i(z)}{dz} &= -y_i V_i, 0 \leq z < h, i = 2\end{aligned}\tag{C.1}$$

which yields the one dimensional wave equation

$$\left(\frac{d^2}{dz^2} + k_i^2 \right) I_i(z) = 0\tag{C.2}$$

The solutions to the wave equation are given as

$$\begin{aligned}I_1(z) &= A_1 \cos(k_1(h_1 + z)) + B_1 \sin(k_1(h_1 + z)), \\ V_1(z) &= jA_1 Z_{c1} \sin(k_1(h_1 + z)) - jB_1 Z_{c1} \cos(k_1(h_1 + z)), \\ &\text{where } -h \leq z < 0, \text{ and} \\ I_2(z) &= A_2 \cos(k_2(h_2 - z)) + B_2 \sin(k_2(h_2 - z)), \\ V_2(z) &= -jA_2 Z_{c2} \sin(k_2(h_2 - z)) + jB_2 Z_{c2} \cos(k_2(h_2 - z)), \\ &\text{where } 0 \leq z < h, \text{ and}\end{aligned}\tag{C.3}$$

where $\sqrt{\frac{-z_i}{y_i}} = jZ_{ci}$ and Z_{ci} is the characteristic impedance of the section of transmission line

defined by i . The boundary conditions are

$$\begin{aligned}z = -h : I_1(-h) &= 0 \rightarrow A_1 = 0, \\ z = 0 : I_1(0^-) &= I_2(0^+), V_2(0^+) - V_1(0^-) = v_0^e, \\ z = h : I_2(h) &\rightarrow A_2 = 0\end{aligned}\tag{C.4}$$

where v_0^e is the delta source voltage. With the boundary conditions we can solve the unknown coefficients B_1 and B_2 to give the input impedance and current distribution

$$\begin{aligned}I(z) &= B_1 \sin(k_1(h_1 + z)), -h_1 \leq z < 0, \\ I(z) &= B_2 \sin(k_2(h_2 + z)), 0 \leq z < h_2,\end{aligned}\tag{C.5}$$

where $B_1 = \frac{-jv_0^e}{Z_{c1} \cos(k_1 h_1) + Z_{c2} \cos(k_2 h_2)} \frac{\sin(k_1 h_1)}{\sin(k_2 h_2)}$

$$B_2 = B_1 \frac{\sin(k_1 h_1)}{\sin(k_2 h_2)}$$

The input impedance is thus, with $v_0^e=1$,

$$Z_{in} = 1/I(0) = \frac{1}{B_1 \sin(k_1 h_1)} = \frac{1}{B_2 \sin(k_2 h_2)} \quad (\text{C.6})$$

APPENDIX C2

Extracting the input impedance of a symmetric insulated dipole antenna using ABCD parameters

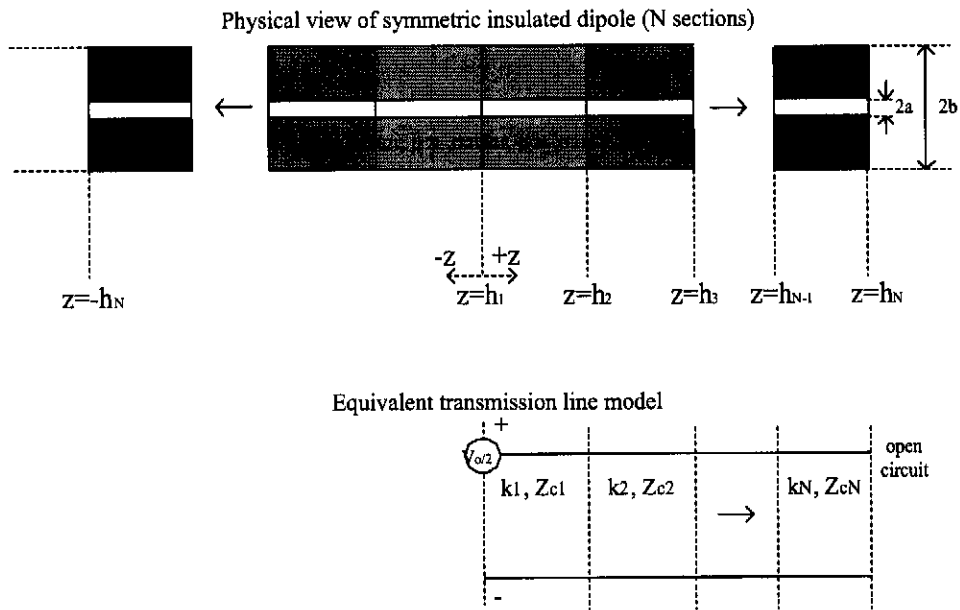


Figure C2-1: Transmission line model : Symmetric insulated dipole with multiple sections

The *ABCD* parameters of a two-port circuit are defined by the input and output current and voltages and can be written in matrix format as follows:

$$\begin{bmatrix} V_{in} \\ I_{in} \end{bmatrix} = \begin{bmatrix} A & B \\ C & D \end{bmatrix} \begin{bmatrix} V_{out} \\ -I_{out} \end{bmatrix} \quad (C.1)$$

where V_{in} and I_{in} are the input voltage and current defining a two-port section,

V_{out} and I_{out} are the output voltage and current defining a two-port section.

To find the total *T matrix* defining a group of multiple sections linked together as illustrated in Figure C2.1, we only multiply the individual *T matrices* of each section with the previous section as follows:

$$\begin{aligned}
\begin{bmatrix} V_{in_total} \\ I_{in_total} \end{bmatrix} &= \begin{bmatrix} A_1 & B_1 \\ C_1 & D_1 \end{bmatrix} \begin{bmatrix} A_2 & B_2 \\ C_2 & D_2 \end{bmatrix} \cdots \cdots \begin{bmatrix} A_N & B_N \\ C_N & D_N \end{bmatrix} \begin{bmatrix} V_{out_total} \\ -I_{out_total} \end{bmatrix} \\
\begin{bmatrix} V_{in_total} \\ I_{in_total} \end{bmatrix} &= \begin{bmatrix} A_{total} & B_{total} \\ C_{total} & D_{total} \end{bmatrix} \begin{bmatrix} V_{out_total} \\ -I_{out_total} \end{bmatrix}
\end{aligned} \tag{C.2}$$

The order in which the *T matrices* are multiplied together must follow the order of the sections. We can implement lumped series resistors between corresponding sections to simulate a loading profile. From the boundary conditions we know that $I_{out_total} = 0$, due to the open circuit after the last section. Thus $B_{total} = D_{total} = 0$. The input impedance of the symmetric insulated dipole is given by

$$\frac{V_{in_total}}{I_{in_total}} = \frac{A_{total}}{C_{total}} \tag{C.3}$$

APPENDIX D1

Pulse receiving characteristic for different percentage Wu-King loadings

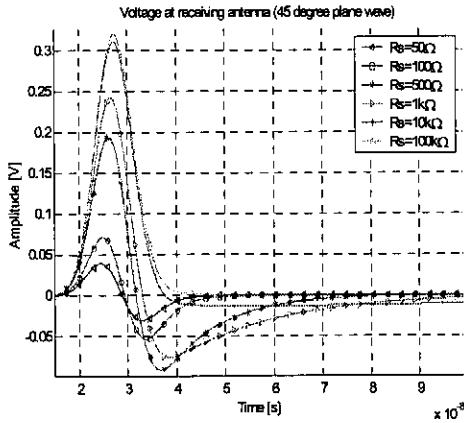


Figure D1-1 : Voltage transient at source for 50% Wu-King dipole (45° plane wave incidence)

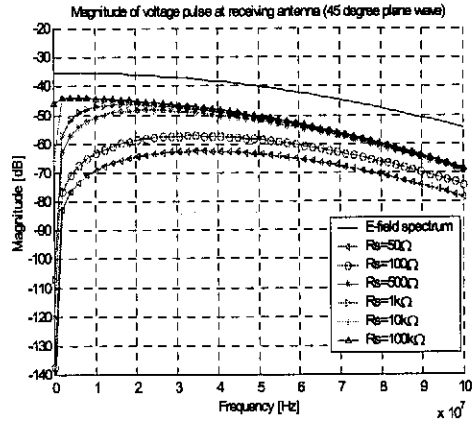


Figure D1-2 : Frequency spectrum of voltage transient at source for 50% Wu-King dipole (45° plane wave incidence)

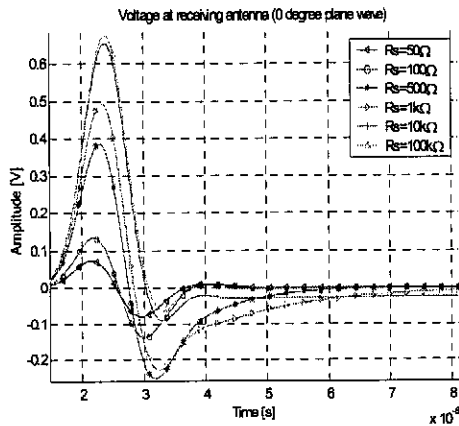


Figure D1-3 : Voltage transient at source for 25% Wu-King dipole (0° plane wave incidence)

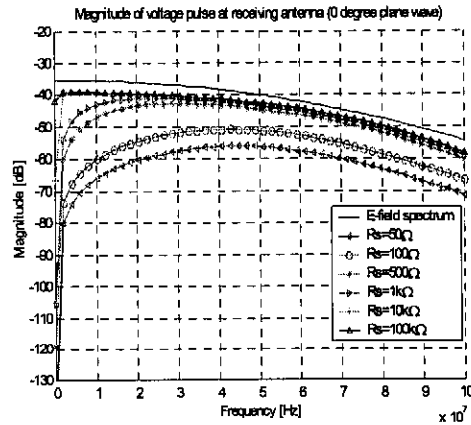


Figure D1-4 : Frequency spectrum of voltage transient at source for 25% Wu-King dipole (0° plane wave incidence)

APPENDIX D2

Input impedance of asymmetrical resistive dipole for different ambient properties

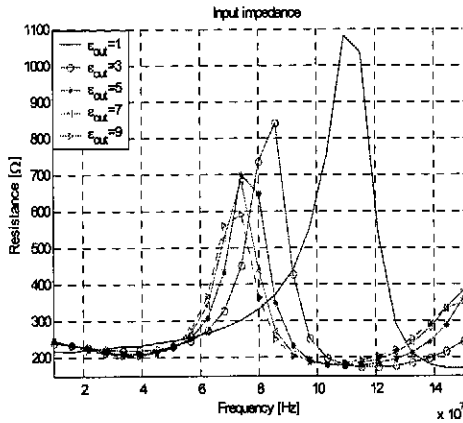


Figure D2-1 : Input resistance of centre-insulated asymmetric resistive dipole ($\epsilon_{in} = 3.7, \sigma_{in} = 0, \epsilon_{out} = 1; 3; 5; 7; 9, \sigma_{out} = 0$)

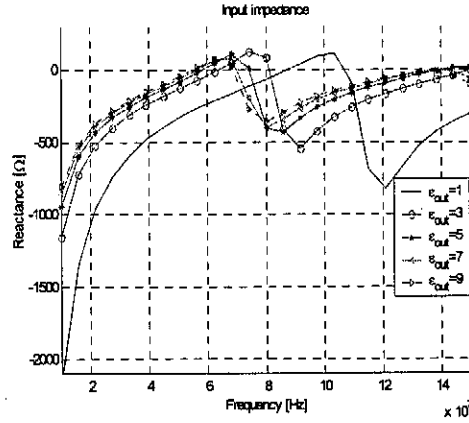


Figure D2-2 : Input reactance of centre-insulated asymmetric resistive dipole ($\epsilon_{in} = 3.7, \sigma_{in} = 0, \epsilon_{out} = 1; 3; 5; 7; 9, \sigma_{out} = 0$)

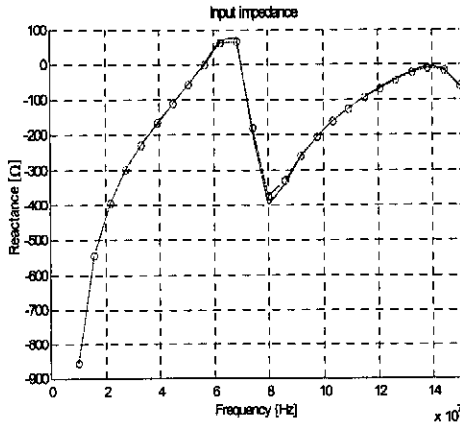


Figure D2-3 : Input resistance of resistive insulated asymmetric antenna with and without an ambient loss factor

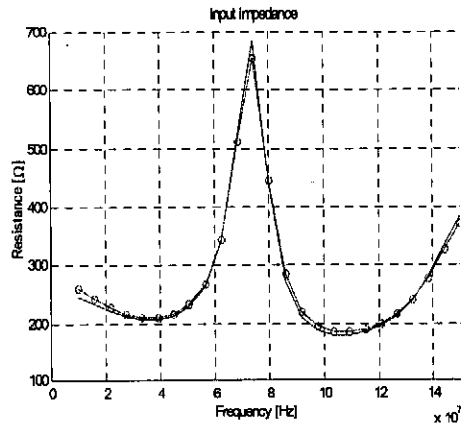


Figure D2-4 : Input reactance of resistive insulated asymmetric antenna with and without an ambient loss factor

APPENDIX D3

Pulse-receiving characteristic for different percentage Wu-King loadings on the asymmetrical dipole

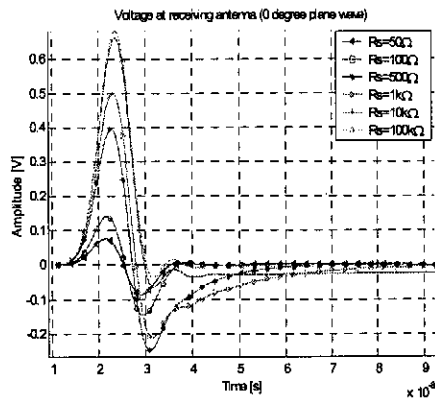


Figure D3-1 : Voltage transient at source for 50% asymmetric Wu-King dipole (0° plane wave incidence)

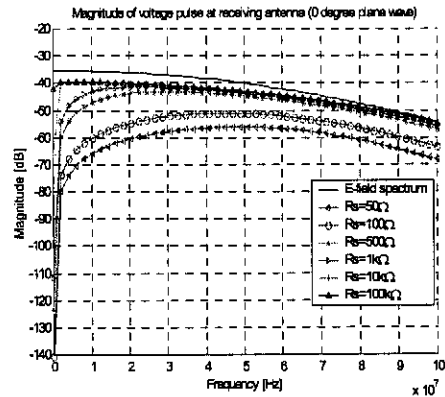


Figure D3-2 : Frequency spectrum of voltage transient at source for 50% asymmetric Wu-King dipole (0° plane wave incidence)

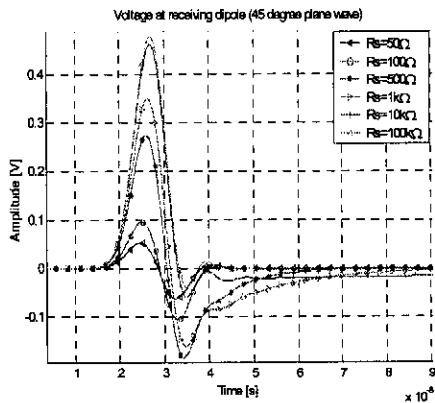


Figure D3-3 : Voltage transient at source for 50% asymmetric Wu-King dipole (45° plane wave incidence)

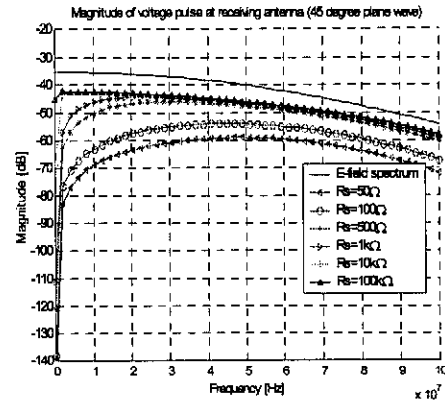


Figure D3-4 : Frequency spectrum of voltage transient at source for 50% asymmetric Wu-King dipole (45° plane wave incidence)

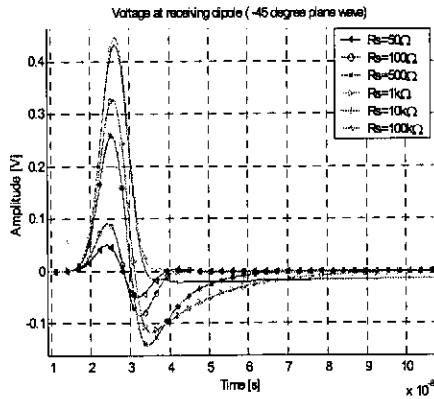


Figure D3-5 : Voltage transient at source for 50% asymmetric Wu-King dipole (-45° plane wave incidence)

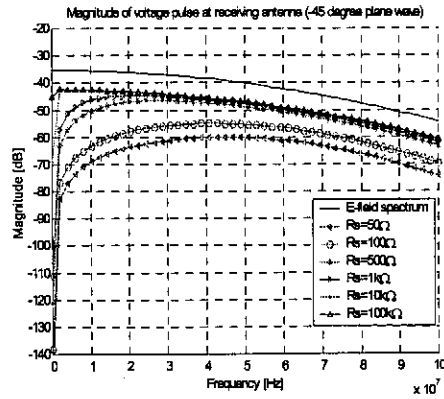


Figure D3-6 : Frequency spectrum of voltage transient at source for 50% asymmetric Wu-King dipole (-45° plane wave incidence)

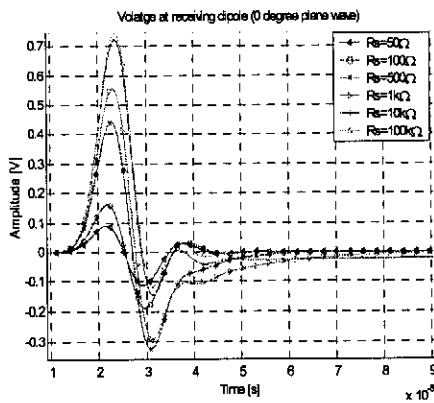


Figure D3-7 : Voltage transient at source for 25% asymmetric Wu-King dipole (0° plane wave incidence)

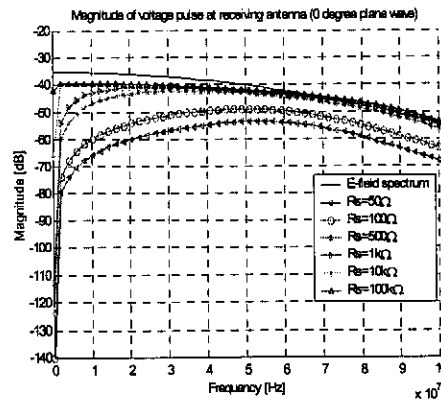


Figure D3-8 : Frequency spectrum of voltage transient at source for 25% asymmetric Wu-King dipole (0° plane wave incidence)